Investigating The $M_{GCS} - M_h$ Relation in High Mass Galaxies

Investigating The $M_{GCS} - M_h$ Relation in High Mass Galaxies

By Veronika Dornan,

A Thesis Submitted to the School of Graduate Studies in the Partial Fulfillment of the Requirements for the Degree Master of Science

McMaster University
Master of Science (2021)
Hamilton, Ontario (Department of Physics and Astronomy)

TITLE: Investigating The $M_{GCS} - M_h$ Relation in High Mass Galaxies
AUTHOR: Veronika Dornan (McMaster University)
SUPERVISOR: Dr. William E. Harris
NUMBER OF PAGES: ix, 71

Abstract

This thesis aims to better constrain the high-mass end of the globular cluster system - halo mass ($M_{GCS} - M_h$) relation. This relation between the total mass contained in the globular clusters in a galaxy and the mass of its dark matter halo has been found to be nearly linear. The measured mass ratio between M_{GCS} and M_h, defined as η, has been found to be constant over a large range of galaxy masses, however there is comparatively less data for galaxies with dark matter halo masses $M_h > 10^{13} M_\odot$. This research analyzes the globular cluster systems (GCSs) of a sample of eleven high-mass brightest cluster galaxies (BCGs) through the use of the photometry program DOLPHOT on Hubble Space Telescope (HST) images in the F814W filter. The mass of the galaxies' GCSs were calculated from their GC radial distributions, and the dark matter halo masses were determined from the known relationship between total stellar mass and halo mass for BCGs. This research utilizes a new standardization technique to calculate the size of the GCS based on the galaxy's virial radius. These GC and halo masses were then compared to determine η at this high-mass end, which was found to be $\eta = (6.84 \pm 0.10_{internal} \pm 1.37_{external}) \times 10^{-5}$. When adding the sample BCGs to a catalogue of 303 lower-mass galaxies a total value for η was found to be $\eta = (2.99 \pm 0.06) \times 10^{-5}$, which is within the literature range for of η, and is both slightly higher and has a reduced uncertainty compared to the value for the catalogue galaxies alone which was found to be $\eta = (2.87 \pm 0.11) \times 10^{-5}$. This consistency between the η-values of high-mass and lower-mass galaxies implies that in order for these BCGs to have such massive GCSs, a large proportion of these GCs must be accreted from galaxy mergers at late redshift.

Acknowledgements

I'd like to thank my supervisor Dr. Bill Harris for providing the attention and support I needed to complete this research and to gain the skills I need to continue in astronomy. Thank you for your patience and understanding as I tried to navigate getting my master's through a pandemic, and for the baked goods at big group meetings. Many thanks to Dr Alison Sills and Dr Laura Parker as well for providing valuable feedback on this research during my committee meetings. I'd like to also thank Claude and Kate for being amazing group members and officemates and always lending me a helping hand (or snack) when I needed one. Finally, I want to thank Jeremy for always being by my side and helping me get through the most stressful parts of this thesis. I probably could have done it without you, but I definitely wouldn't have wanted to.

Contents

List of Figures

List of Tables

Chapter 1

Introduction

1.1 Globular Clusters

Globular clusters (GCs) are roughly spherical, gravitationally bound groups of ancient stars found in the haloes of galaxies. Compared to other types of star clusters, such as young massive clusters (YMCs) or open clusters, GCs are older, containing numbers of stars on the order of $10^4 - 10^7$ (Beasley 2020). GCs are also some of the oldest structures observed in the universe, and can be up to 13 billion years old (VandenBerg et al. 2013), making them very useful as tracers of galaxy formation mechanisms at high redshift. The total number of GCs in a galaxy, referred to as the GC system (GCS), varies with the size of the host galaxy, where a galaxy the size of the Milky Way can have a hundred or more GCs, dwarf galaxies may only have a handful, and extremely massive brightest cluster galaxies (BCGs) can have as many as 10s of thousands (Beasley 2020).

Although our understanding of how GC formation relates to dark matter content in early galaxy formation is still being explored, the current theories of GC formation mechanisms generally agree on two main groups of models: GC formation as a natural byproduct of active star formation at high redshifts, and GC formation associated with special conditions in low-mass dark matter halos. For the first model of GC formation, it is understood that the conditions in gas-rich galaxies at high redshift would be favourable

to GC formation due to the high gas pressures in the turbulent ISM. This allows for high maximum mass scales for gravitational collapse, which would in turn enable the formation of giant molecular clouds (GMCs) that are able to overcome shear, centrifugal forces, and feedback. A certain fraction of these clouds would then have pockets of gas and dust collapse to then form massive clusters of stars, which due to the highly turbulent and high-pressure environment present at high redshift, results in these massive clusters having high masses and densities, thus allowing them to remain gravitationally bound for over a Hubble time, as we observe (Li and Gnedin 2014, Boylan-Kolchin 2017, Reina-Campos and Kruijssen 2017, Howard et al. 2018, Choksi and Gnedin 2019, Lahén et al. 2020, Lim et al. 2020).

The second group of theories of GC formation is linked to dark matter halo assembly, and is much less consistently agreed upon than GC formation as a byproduct of star formation. There are several different ways to approach this, and all still remain relatively qualitative, with more work needed to develop them. Most of these works focus on potential GC formation within dark matter mini-halos with characteristic masses on the order of $10^8 M_\odot$. The earliest work on this topic comes from Peebles and Dicke (1968), which argued that GCs formed as gravitationally bound gas clouds that predated the formation of their host galaxies. Another one of these theories comes from Trenti et al. (2015), who proposed that mergers of these mini-halos which are gas-rich and star-free can lead to shock-induced compression and formation of star clusters in the central regions of the mini-halos. These star clusters would then be stripped of the DM "envelope" surrounding them, resulting in the populations of GCs we see in galaxies today. A more recent take on this school of thought comes from Madau et al. (2020), which attributes GC formation to a more specialized dynamical model of high gas pressure star formation that is triggered by high speed collisions between DM subhalos during the host galaxy formation. These theories of GC formation and evolution are especially interesting when considering the observational relation that is seen between

current GC populations and dark matter halos, as is discussed in section 1.2.

An important, fundamental property of GC systems across host galaxies is its GC luminosity function (GCLF). The GCLF is the number of GCs per unit magnitude or luminosity within the GCS, and has been found to have a nearly universal log-normal shape across galaxy masses and morphologies (Harris et al. 2014). Jordán et al. (2007) and Villegas et al. (2010) also investigated this luminosity function over a large range of galaxy masses and came to the consistent conclusion that there, indeed, is small variation in this GCLF. This log-normal distribution is represented in the I-band through equation 1.1, where L_o is the turnover luminosity, σ_L is the Gaussian dispersion, and N_o is a free parameter constrained by the number of GCs (Harris et al. 2014).

$$\frac{dN}{d\log L} = N_o exp\left[- \frac{(\log L - \log L_o)^2}{2\sigma_L^2} \right] \tag{1.1}$$

It was found in Harris et al. (2014) that the turnover luminosity for BCGs corresponds to $M_I = -9.0$ quite consistently, and this characteristic of the GCLF can be very useful in helping determine the number of GCs in a system. This is discussed in more detail in chapter 2, section 2.3.2.

1.2 $M_{GCS} - M_h$ Relation

It has been known, and discussed in the literature, for several decades now that there exists a strong relationship between the mass of the globular cluster system of a galaxy (M_{GCS}), and the total mass of the galaxy, which is dominated by the dark matter halo mass (M_h) (Blakeslee et al. 1997). Since it was first discovered, this result has been investigated and reproduced multiple times, including by Blakeslee (1999), Hudson et al. (2014), Harris et al. (2015), and among many others, which will be discussed in the following subsections. It has been found that this relationship is linear across all types

of galaxies and mass ranges that have been investigated, taking the form of equation 1.2 (Harris et al. 2017).

$$\langle \eta_M \rangle = \left\langle \frac{M_{GCS}}{M_h} \right\rangle = 2.9 \times 10^{-5} \tag{1.2}$$

The exact value of η_M varies depending on the methods used to determine galaxy GCS and halo masses or the sample of galaxies used, but has found itself quite consistently in the range of $2.5 \times 10^{-5} - 4.0 \times 10^{-5}$ since 2014 (Harris et al. 2015). A visual illustration of this η_M relationship can be seen in figures 1.1 and 1.2, both taken from Harris et al. (2015). As can be seen, the range of galaxy halo masses investigated spans from $10^{10} - 10^{14} M_\odot$, with noticeably less data available for brightest cluster galaxies (BCGs) above $10^{14} M_\odot$ comparatively.

1.2.1 Observational History of The $M_{GCS} - M_h$ Relation

Research on this mass relation was first done by Blakeslee et al. (1997) and Blakeslee (1999), in which 24 giant galaxies in Abell clusters were investigated, and had the number of GCs determined using a similar photometry method as this research (see chapter 2), but determined the galaxies' total masses, dominated by dark matter, through halo X-ray temperature or velocity dispersion. This research showed that a direct relation between N_{GC} and M_h existed with a nearly constant ratio between the two values, but due to the restrictiveness of the sample used, with this study only probing massive galaxies in rich clusters, it could not be applied to all galaxies generally.

The next major step in expanding our understanding of this relation came a decade later by Spitler et al. (2008), who used a sample of 25 giant galaxies, of a wider range of masses and environments than Blakeslee et al. (1997), again showed that N_{GC} and M_h had a nearly constant ratio. This work was then continued soon after by Spitler and Forbes (2009) with a sample of over 100 galaxies, and for the first time changed

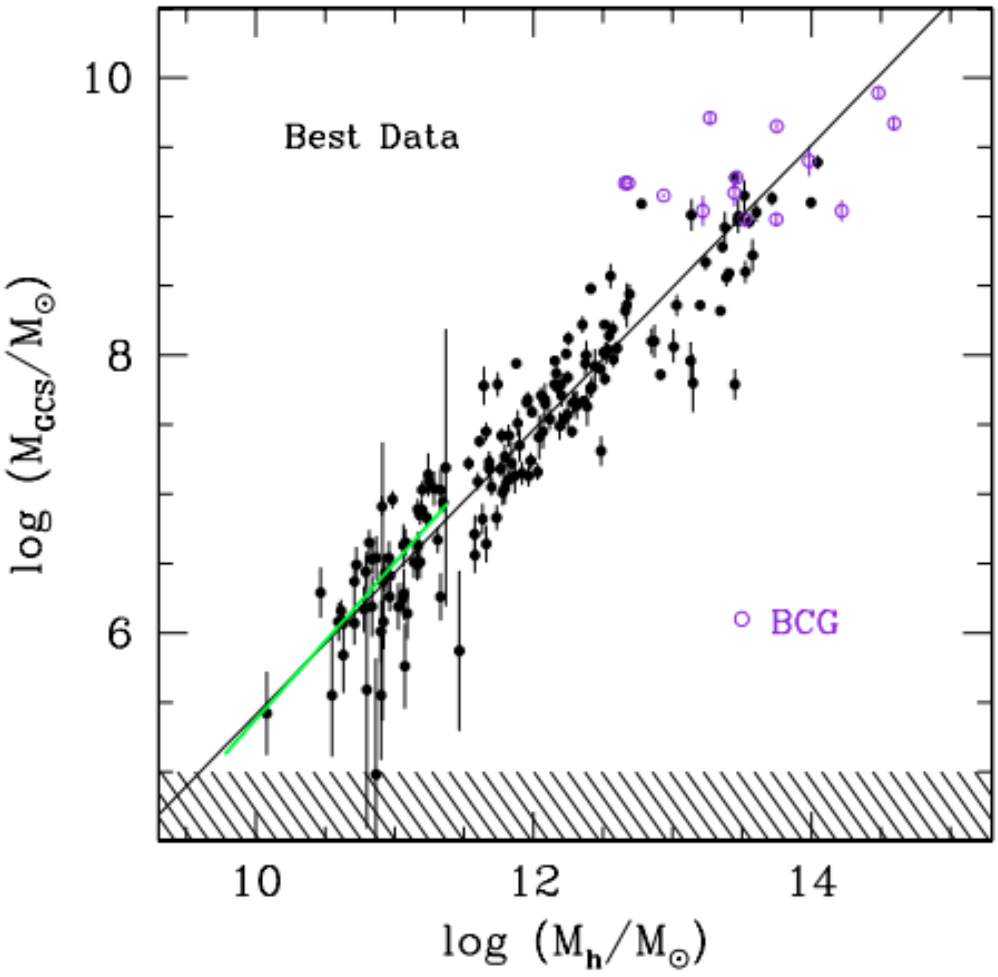

FIGURE 1.1: M_{GCS} vs M_h for what was determined to be the "best" sub-sample of 175 galaxies. The green line represents the η_M prediction from Kravtsov and Gnedin (2005), and the shaded region represents the mass range at which M_{GCS} values are too small to be reliable. Reprinted by permission of the AAS and the authors of W. E. Harris et al. (June 2015). Dark Matter Halos in Galaxies and Globular Cluster Populations. II. Metallicity and Morphology. *Astrophysical Journal* 806(1) 36, 36.

the focus of the relation from the relationship between the number of GCs and the halo mass, to that between the mass of the GCS and the halo mass. This shift to comparing masses was particularly interesting due to the fact that average GC mass is not constant across galaxies, but increases slightly with total galaxy luminosity (Harris et al. 2017),

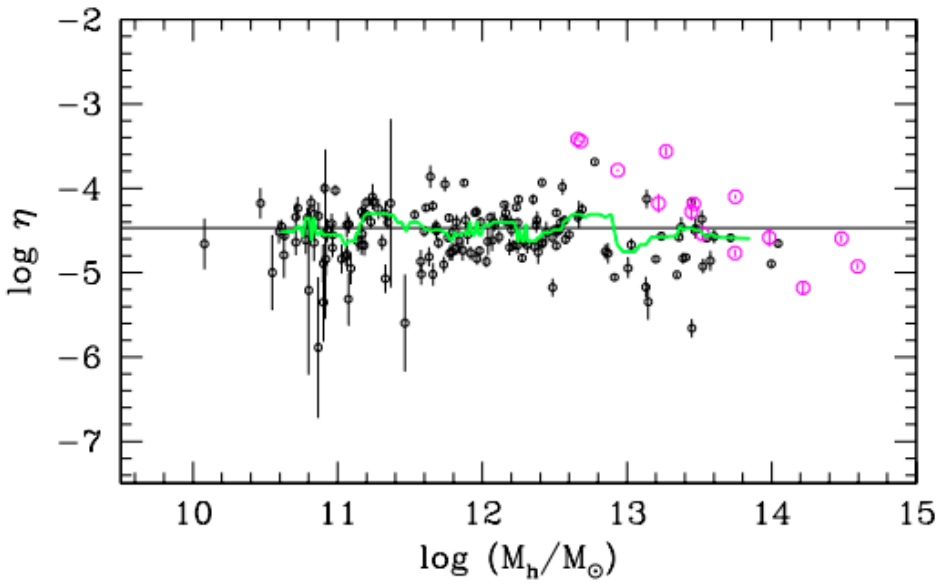

FIGURE 1.2: Ratio of M_{GCS} to M_h plotted against $M_h$for what was determined to be the "best" sub-sample of 175 galaxies. The green line is a binned running median η, and the magenta circles are BCGs. Reprinted by permission of the AAS and the authors of W. E. Harris et al. (June 2015). Dark Matter Halos in Galaxies and Globular Cluster Populations. II. Metallicity and Morphology. *Astrophysical Journal* 806(1) 36, 36.

as is shown in equation 2.3 in section 2.3.2.

Georgiev et al. (2010) continued to expand the total number of galaxies investigated by determining the N_{GC} for dwarf galaxies that they had worked with previously, along with other galaxies from the literature, and also determined these galaxies' stellar and gas masses. Using these values, they defined the specific GCS mass as $S_M = M_{GCS}/(M_\star + M_{gas})$, where here the denominator represents the baryonic mass of the galaxy. Georgiev et al. (2010) then used both dynamical mass measurements of dwarf galaxies and galaxy group dynamics to convert their S_M to $\eta = M_{GCS}/M_h$.

These previous samples of galaxies in the literature were then combined by Harris et al. (2013) into a catalogue of N_{GC} data from 419 galaxies in total, and was used to

calculate M_{GCS} for those that had not taken the step already to convert numbers of GCs to masses of the systems. This was followed closely by Harris et al. (2014) which then used the same method discussed in section 2.4 to determine the halo masses for the galaxies in the previous catalogue, to determine a value for η based on a more broad and numerous sample than was done previously. Harris et al. (2015) then used the 2013 catalogue to determine the role galaxy morphological types and GC metallicity have on η, finding there is no first-order dependence on morphology, and that the mass relation still holds for both metal rich and metal poor GC subpopulations, although with differing η-values; $M_{GCS,blue} \sim M_h^{0.96}$ for metal-poor and $M_{GCS,red} \sim M_h^{1.21}$ for metal-rich (Harris et al. 2015).

Harris et al. (2017) again investigated the $M_{GCS} - M_h$ relation for extreme situations, this time for galaxy clusters and for Ultra-Diffuse Galaxies (UDGs) in the Coma cluster. They also took the opportunity to re-calibrate the η ratio to obtain an average value across galaxies of $\langle\eta\rangle = 2.9 \times 10^{-5}$, and an average value for galaxy clusters to be slightly higher at $\langle\eta\rangle = 3.9 \times 10^{-5}$. They also found that the UDGs investigated had η-values consistent with the overall $M_{GCS} - M_h$ relation.

This mass relation was extended to GCS and dark matter halo sizes by Hudson and Robison (2018), which looked at radial density profiles of GC systems around galaxies in group environments. Nine galaxies in four groups were studied, and when combining their results from those from the literature discussed above, they found a steep, yet non-linear, relationship between the effective radius of the GCS ($R_{e,GCS}$) and the virial radius of the halo (R_{200}). This relation was found to take the form $R_{e,GCS} \propto R_{200}^{(2.5-3.0)}$. This work showed that the relationship between the GC system of a galaxy and its dark matter halo is connected in multiple ways.

Prior to this point in the literature, few galaxies with halo masses less than $10^{10} M_\odot$ have been investigated and applied to this mass relation, as is apparent in

figure 1.1. This is in part due to the fact that methods of determining dark matter halo mass based on weak lensing used in previous works cannot be reliably applied to dwarf galaxies, so Forbes et al. (2018) determines new halo masses from HI gas kinematics for a sample of dwarf galaxies. They found that the $M_{GCS} - M_h$ relation held for dwarf galaxies with masses down to $10^9 M_\odot$, although with much more scatter than for higher masses, assuming these galaxies hosted GCs as some studied did not.

Most recently, Prole et al. (2019) studied 175 low surface-brightness (LSB) galaxies in the Fornax cluster which, similarly to dwarf galaxies, cannot have weak lensing based methods applied to them to determine halo mass due to the low number of LSB galaxies available since weak lesnsing is a stacking measurement. Instead, this was the first instance in which the $M_{GCS} - M_h$ relation was applied to determine a sample of galaxies' halo masses from their GCS masses, showing how useful this relation can be as it is better constrained for all mass ranges.

1.2.2 Theoretical History of The $M_{GCS} - M_h$ Relation

Theoretical literature contributions to the the $M_{GCS} - M_h$ relation have also been made relating what is known about the relation to theories of GC and early galaxy formation, the earliest of these contributions being Diemand et al. (2005) and Moore et al. (2006). In these works the authors used high-resolution cosmological N-body simulations to find a relation between amount of material collected in high-σ peaks and the mass of the virial halo for galaxies at very high redshift ($z \sim 12$), in which the amount of material increases by roughly $M_h^{1.2}$. These high-σ peaks in which the material is collected should be the places where proto-GCs begin to form, and because of this the very old, metal-poor GC populations should increase with host galaxy halo mass.

At the same time, Kravtsov and Gnedin (2005) also looked at the relation between GC formation and early galaxy formation for a Milky Way-type galaxy starting at roughly the same redshift as the previous work which was discussed, using a

high-resolution hydrodynamic simulation. Although this simulation did not resolve individual GCs, potential sites of GC formation were identified as cores with densities above $1 M_{\odot} pc^{-3}$ in the emerging giant molecular clouds (GMCs). The results of this work find that the total GCS masses relate to the masses of the host subhalos following the form $M_{GCS} \sim M_h^{1.13 \pm 0.08}$, taken from the range of simulated halo masses between $6 \times 10^9 M_{\odot} - 3 \times 10^{11} M_{\odot}$.

These simulations have provided theoretical evidence supporting the linearity of the $M_{GCS} - M_h$ relation, however the results of the simulation done by Bekki et al. (2008) did not agree with this. In this work the authors aimed to find GCs at formation times using a cosmological simulation by defining proto-GCs as central particles in virialized sub-halos. This simulation was applied to multiple model galaxies of varying sizes, and yielded a scaling relation between number of GCs and halo mass of the form $N_{GC} \sim M_h^{1.3}$, which is steeper than the results of other work on this relation.

After almost a decade, the next substantial theoretical contribution to the understanding of the $M_{GCS} - M_h$ relation came from El-Badry et al. (2019) and Choksi and Gnedin (2019), which used analytic and semi-analytic models, respectively, to investigate the behaviour of the mass relation, and to determine the conditions required to form these GC systems. Both works found that the $M_{GCS} - M_h$ relation was overall linear, but more sensitive to GC formation processes for galaxies with $M_h \lesssim 10^{11.5} M_{\odot}$, with Choksi and Gnedin (2019) finding that below this mass the relation is steeper than directly proportional. Choksi and Gnedin (2019) also found that the contribution of accreted satellite galaxies to the GC systems is a strong function of the host galaxy mass, from 0% on the low mass end, to as high as 80% for the highest masses.

The next theoretical contribution was that of Bastian et al. (2020) who created a simulation of a cosmological volume using E-MOSAICS which considered GC formation and evolution within a detailed galaxy formation model. E-MOSAICS is a suite of

galaxy formation simulations run with the EAGLE model that include the MOSAICS semi-analytic model for star cluster formation and evolution (Pfeffer et al. 2018). From this model, which they used to look at the GC populations of 1707 simulated galaxies with halo masses above $10^8 M_\odot$, they found that the $M_{GCS} - M_h$ relation remained linear, with $\eta \sim 5 \times 10^{-5}$, for galaxies with halo masses above $\sim 5 \times 10^{11} M_\odot$, and that below this mass they predict a downturn in the mass relation.

The most recent research into this mass relation comes from Doppel et al. (2021), who used the Illustris simulation to determine how accurate GC-based halo mass estimates are, like those done by Prole et al. (2019), discussed in section 1.2.1. This research focused on galaxies with stellar masses between $10^8 - 10^{11.8} M_\odot$ which were identified in 9 simulated Virgo-like clusters, and found that GC-based halo masses estimated were, on average, reliable for systems with at least 10 GCs. This result is promising for the use of the $M_{GCS} - M_h$ relation in the future.

1.3 $M_\star - M_h$ Relation

One of the reasons why the $M_{GCS} - M_h$ relation is so compelling and unique to GCs in particular, is the fact that another strong M_h relationship, that links total stellar mass and halo mass is decidedly non-linear. This relation is shown visually in figure 1.3 (Hudson et al. 2015), and the difference in shape can be seen clearly when compared to figure 1.2. This relation is also shown mathematically in equation 1.3, where M_1 is a characteristic halo mass, f_1 is the stellar mass - halo mass ratio at the characteristic mass, and β and γ are fitting parameters (Hudson et al. 2015). Equation 1.3 can be seen again in chapter 2, section 2.4, with values determined for those parameters from Harris et al. (2020).

$$M_\star / M_h = 2 f_1 \left[\left(\frac{M_\star}{M_1} \right)^{-\beta} + \left(\frac{M_\star}{M_1} \right)^{\gamma} \right]^{-1} \tag{1.3}$$

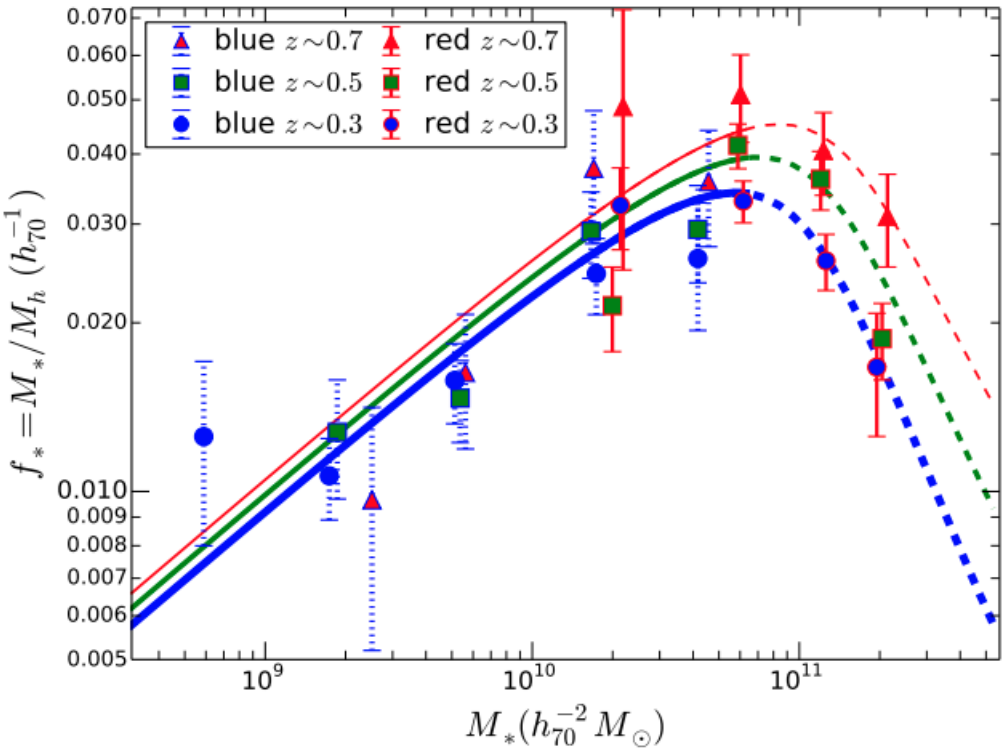

FIGURE 1.3: $M_\star/M_h$ vs $M_\star$ determined using weak-lensing of a range of galaxies in the CFHT Legacy Survey. The legend refers to galaxy redshifts and galaxy stellar population metallicity. Reprinted from M. J. Hudson et al. (Feb. 2015). CFHTLenS: co-evolution of galaxies and their dark matter haloes. *Monthly Notices of the Royal Astronomical Society* 447(1), 298–314.

This $M_\star - M_h$ relation holds strongly for high-mass galaxies, particularly for BCGs like those being investigated in this research (see chapter 2). This means that equation 1.3 can be used to reliably determine the halo masses of massive galaxies when their total stellar masses are known. It should be noted here that, although this relation is straightforward when applied to BCGs such as those in this research, when it is applied to a satellite galaxy in a group or cluster this relation will yield a mass closer to the M_h the satellite galaxy had before falling into the bigger group and getting partially stripped. Thus, for satellite galaxies this relation connects the current $M_\star$ to the M_h at the time of origin (Hudson et al. 2015).

1.4 Motivation of This Research

As can be seen in figure 1.1, although there are many measurements for galaxies with halo masses between $10^{10}M_{\odot}$ and $10^{13}M_{\odot}$, there are far fewer above $10^{13}M_{\odot}$, and those that are available have a greater amount of scatter around the linear fit of the relationship. A likely source of this scatter may be the fact that the masses of these high-mass galaxies have been determined using different photometry techniques, since they are drawn from multiple catalogues. Another important factor that may be influencing this scatter, particularly the BCGs, is the fact that there is no clear boundary between GCs associated with BCGs and those associated with the intracluster medium surrounding these galaxies, and as such, differing catalogues may define different GCS boundaries for BCGs. No single, consistent procedure has been applied to determining M_{GCS} values for these bright galaxies and the behaviour of η_M at these high masses needs to be better constrained in order to determine if this relationship holds as strongly for extremely high-mass galaxies as it does for those with lower halo masses.

The high-mass end of the $M_{GCS} - M_h$ relation could be better understood if more galaxies with halo masses above $10^{13}M_{\odot}$ were added, and if more firmly consistent methodology was applied to determine both their masses, and the boundaries of their GCSs. This research aims to do just that, by determining the M_{GCS} and M_h using a uniform technique for a sample of BCGs, as will be outlined in section 2. Once the understanding of how η_M behaves in this high-mass range is improved through adding in this BCG sample to the broader catalogue of galaxies, the results can be compared to the theory and simulations proposed in the literature, discussed in section 1.2, and insights may be gained about what this means for massive galaxy formation mechanisms at high redshift.

Chapter 2

Methods

In this chapter I will discuss the methods used to obtain the GCS and halo masses for a sample of eleven BCG galaxies, as well as how these galaxies were selected for the sample. An overview of the photometry programs used in the research (originally DAOPHOT, but ultimately DOLPHOT) will also be discussed here, as well as of how they work.

2.1 The Galaxy Sample

The sample of galaxies in this research were selected with some specific considerations in mind. The first, and most obvious, was the mass range. Since this research aims to better constrain the high-mass end of the $M_{GCS} - M_h$ relation, only galaxies with halo masses on the order of $10^{13} M_\odot$ or higher are of use. The second consideration was consistency, since an ideal sample would have images of each of the galaxies taken with the same instruments, in the same filter, and ideally would have similar exposure times, similar distances and be located in similar areas of the sky.

With these considerations taken into account, an appropriate sample of galaxies was determined to be those in HST proposal ID 10429 (Blakeslee 2004). This proposal for images to be taken of a sample of galaxies was originally for the purpose of determining

the galaxies' surface brightness fluctuation distances in order to calculate their infall to the Shapley Supercluster. Although that is not related to this research, the nature of the work done by Blakeslee required massive galaxies within the sample supercluster, so this sample is made up of exclusively brightest cluster galaxies (BCGs), relatively close to one another in the sky, ideal for this research. Because these galaxy images were taken in a single HST observing program, they were all taken with the ACS camera on-board the HST, in the same near-IR filter (F814W), and are readily available on the HST archive. This proposal was also for eleven galaxies, which was also found to be an appropriate size given the time constraints of this work.

Below, in table 2.1, is a list of the target galaxies, their galactic latitudes (b), longitudes (l), extinction in F814W, distance moduli in F814W calculated from the galaxies' CMB velocity and Hubble distance ($H_o = 70 km/s/Mpc$), and their total visual magnitudes. Figure 2.1 shows the HST archive reference images of the galaxies in this sample, for a visual representation. Due to these galaxies being close to one another in the sky, the same Hubble Frontier Field, HFF4, was able to be used for all of the images to determine background object density to be removed from the density distributions of the galaxies, although that will be discussed in more depth in section 2.3.1.

Target Name	l	b	A_I	$(m-M)_I$	M_V^T	$t_{exp}(s)$
J13481399-3322547	316.35°	28.01°	0.082	36.335 ± 0.0033	-21.67	21081.0
J13280261-3145207	311.96°	30.47°	0.079	36.446 ± 0.0045	-22.00	35550.0
J13275493-3132187	311.97°	30.69°	0.076	36.839 ± 0.0039	-23.30	35550.0
J13272961-3123237	311.89°	30.85°	0.088	36.679 ± 0.0037	-23.30	35550.0
ESO 509-G067	314.69°	34.75°	0.103	36.023 ± 0.0091	-23.30	18567.0
ESO 509-G020	312.83°	34.81°	0.086	35.957 ± 0.0073	-23.26	18567.0
ESO 509-G008	312.47°	34.78°	0.080	36.031 ± 0.0042	-22.97	18567.0
ESO 444-G046	311.99°	30.73°	0.076	36.635 ± 0.0044	-24.80	35426.1
ESO 383-G076	316.32°	28.55°	0.083	36.223 ± 0.0039	-24.24	21081.0
ESO 325-G016	314.72°	23.64°	0.123	36.214 ± 0.0035	-22.34	18882.0
ESO 325-G004	314.08°	23.57°	0.092	35.958 ± 0.0042	-23.25	18882.0

TABLE 2.1: List of target galaxies with galactic latitude, longitude, extinction in the F814W filter, distance modulus in the F814W filter, and total visual magnitude.

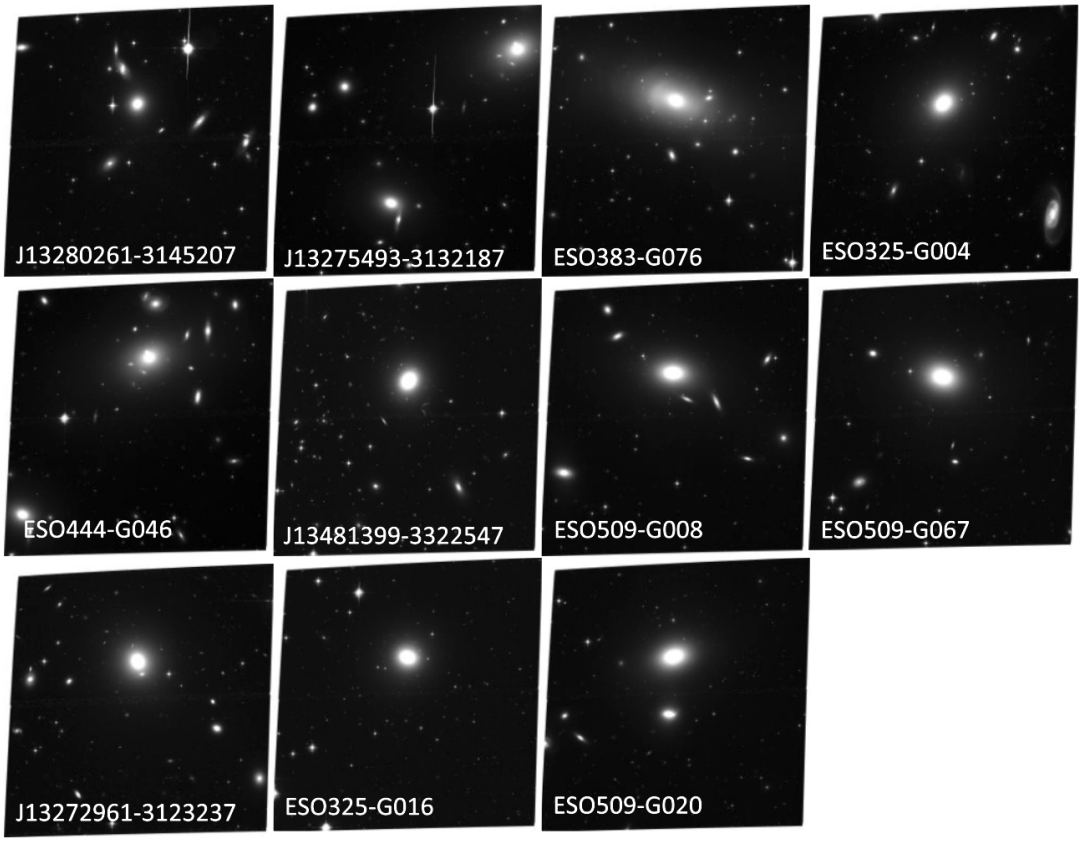

Figure 2.1: HST reference images for the galaxies in this research sample.

2.2 Photometry Programs

In order to identify GCs in the target images, we needed to use a photometry program which would analyze a combined image from the HST archive, and return all of the star-like objects in the image along with important characteristics of those objects, namely their positions and magnitudes. There are two photometry programs that do this well, DAOPHOT, created by Peter Stetson (Stetson 1987), and DOLPHOT, created by Andrew Dolphin (Dolphin 2000).

This research originally used DAOPHOT to perform the photometry process on the first galaxy selected in the sample: 2MASX J13272961-3123237. However, I then switched to DOLPHOT in order to obtain deeper photometric limits on the images, gain better discrimination of non-steller objects, and to have more consistency across all images, as DOLPHOT uses the same PSF for a given camera and filter, which is the same for all galaxies in this sample. DAOPHOT and DOLPHOT are very similar suites of photometry programs, with the main difference being that DAOPHOT requires more user input and DOLPHOT does not. DOLPHOT was then used for the remaining target images in the sample, as well as for a second analysis of 2MASX J13272961-3123237, for both consistency and for a more accurate analysis of that specific target.

2.2.1 Preparing The Images

There are many steps in the process of using DOLPHOT to analyze an image, but the first one is to prepare the image before running DOLPHOT on it. On the HST archive one can access a series of ACS exposures of the target in the form of raw `.flc` images, which are charge transfer efficiency (CTE) corrected. These exposure images will then need to be combined into a single, combined, `.drc` reference image for DOLPHOT with camera field distortion and cosmic ray hits removed. This is done by creating a combined, multidrizzled image from the `.flc` exposures using the `astrodrizzle` function available through `python`, which can be downloaded at: `https://astroconda.readthedocs.io/`

`en/latest/package_manifest.html#/`. This will be referred to simply as "the reference image". Below is an example of the process after having downloaded the `.flc` exposures.

```
import glob

from astropy.io import fits
from drizzlepac import astrodrizzle

input_flcs = glob.glob('*flc.fits')

astrodrizzle.AstroDrizzle(input_flcs,
      output='combined',
      preserve=False,
      driz_sep_bits='64,16',
      driz_cr_corr=True,
      final_bits='64,16',
      clean=True,
      configobj=None,
      combine_type='median',
      combine_nhigh=2,
      build=True,
      final_pixfrac=1.0,
      final_wcs=True,
      final_scale=0.05)
```

This will return the reference image for the target. This reference image gives us the deepest image on which to find target objects. DOLPHOT will then measure this reference image by PSF-fitting on the individual `.flc` exposures that the reference image is made of, average their luminosities, and then convert them to the magnitudes of the objects. This reference image also creates a master coordinate scale across all the exposures, transforming the (x,y) pixel coordinate locations of the objects in the exposures to the reference image pixel coordinate scale. Figure 2.2 shows an example of one of these reference images for 2MASX J13280261-3145207.

The next steps in preparing the images can be done with built-in DOLPHOT routines. First we must mask any bad pixels and multiply by the pixel area mask, using

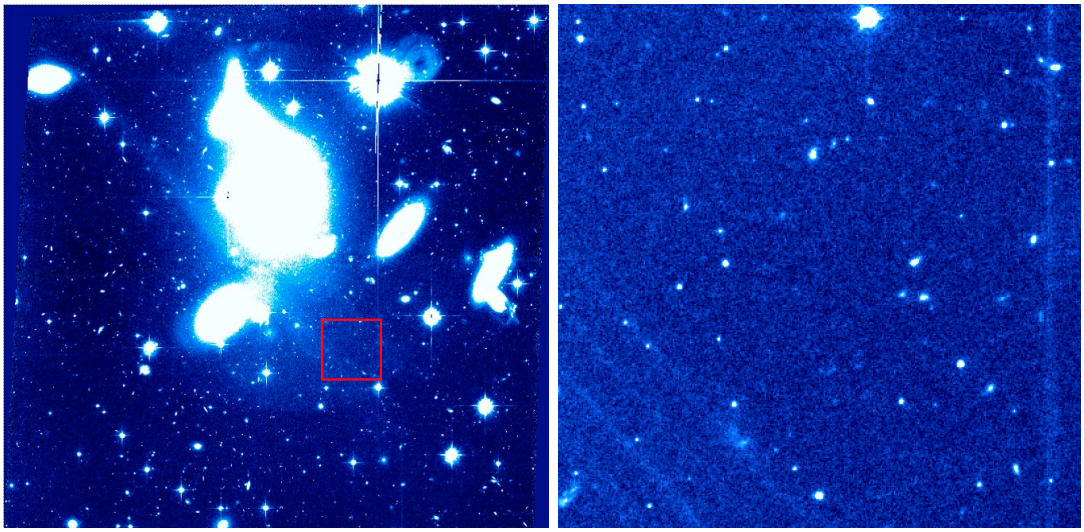

FIGURE 2.2: Combined reference image for 2MASX J13280261-3145207, where the right image is the zoomed in section of the red square in the left image to show individual GCs.

`acsmask` on all the images. This routine reads each image, including both the `.flc` exposures and the reference image, and reads the data image and the data quality image provided by STScI and masks out all of the pixels deemed to be bad. Bad pixels can include those with a decoding error, calibration file defect, permanent camera defect, missing data, unrepaired warm pixel, questionable pixel, and other bad pixel. These masked pixels are then ignored for the rest of the photometry process. This routine also flags all pixels with 3500 or more counts and categorizes them as saturated for later reductions (Dolphin 2000).

The ACS camera has two CCD chips, both embedded in the `.flc` image files, which have slightly different PSFs associated with them, so the next step is to split each `.flc` image into two images, one for each chip. This is done using the DOLPHOT routine `splitgroups` on all the images, which outputs two new images for each exposure, named `*.chip1.fits` and `*.chip2.fits`, although the reference image will only be written to one `.chip1.fits` image.

The final step needed to be taken in preparing the images is calculating their background sky levels. This is done using the DOLPHOT routine `calcsky`, which derives a sky-map for each image, for each CCD chip. This routine is a mean with iterative rejection, meaning the mean and standard deviation of the background sky levels are calculated for each iteration and any values that are above or below determined thresholds are rejected. This process continues until no pixels are rejected. The routine divides the image into a grid of squares with equivalent sizes and calculates the mean and standard deviation of the background sky levels for each square, with the values being assigned to the central pixel of the square. The final sky map of the image is created through interpolation of this grid. In order to do all this the routine requires several parameters to be specified; The length of each side of the grid squares, and the σ_{low} and σ_{high} thresholds. Two other parameters must also be given to the routine to work, inner and outer pixel annuli, but this is for an alternative sky-map calculating method that will not be used here, and these parameters are ignored when grid size is set with a negative number. For consistency, the same parameters are used on all images of all galaxies in the sample: `calcsky <image name> 15 35 -128 2.25 2.00`, the parameters being r_{in}, r_{out}, negative grid length size, σ_{low}, and σ_{high}, in that order (Dolphin 2013). Although this process is required to run DOLPHOT, in the later aperture photometry step the local sky values for each object are used instead of the global sky-map value.

2.2.2 Running DOLPHOT

Now that the images are prepared, the DOLPHOT photometry processes can be run on the images. To do this, two master parameter files for the target image must be created first, one for each chip (this can also be done with one master parameter file for both chips but it was found that running the chips separately was more efficient). These two files are essentially the same with the only changes to the names of the image files and the output files, reflecting the chip the DOLPHOT run is being applied

to. The parameter file states the number of images, then lists them starting with the reference image, and then the individual exposures in the correct chip. The parameters for the DOLPHOT run are then listed, most of which are left as the default, but with some changes made. Some examples of what are set by this parameter file include the aperture size, used later in the aperture photometry step, the degree of sophistication of the coordinate transformations onto the image, the PSF type, and the number of iterations for the fit, among many others. Please see Appendix A for an example of one of these parameter files, with a description of the parameters provided. The parameters used in this parameter file are applied for all images in this sample for consistency.

Once the parameter file is complete, DOLPHOT can be run for chips 1 and 2 separately using the command `dolphot chip*.dat -pchip*.param > output*.log &` where * is either 1 or 2. Here `chip*.dat` is the output data file and `output*.log` is the logfile produced by DOLPHOT, which can have some important information, especially if the program crashes or does not reduce every image before finishing for some reason so the source of the issue can be found. Running this measurement process takes several hours to complete. For the process itself DOLPHOT uses point spread functions (PSFs) taken from the HST archive library for the specific camera and filter used for an image, which in this sample is exclusively the ACS camera in the F814W filter, meaning only two archive PSFs are required, one for each chip. This archive PSF acts as a good initial guess of the properties of the image, which is needed for DOLPHOT to begin the photometry process (Dolphin 2013).

Next, DOLPHOT will search for star-like objects, which will include the GCs in these target galaxies since on the scale of these images GCs are small enough to be unresolved and appear star-like to DOLPHOT. For example, for a GC with half-light diameter of $D_e = 6pc$, at a distance of $150Mpc$, it would have an angular size of just 0.0083 arcseconds, much less than the PSF width of 0.1 arseconds for these images. In the context of DOLPHOT these will be referred to as star-like objects, but when

determining distributions for the galaxies they will be referred to as GCs. For each chip, a two-pass search for star-like objects is done, then followed by an iterative solution. First, for each pass, DOLPHOT analyzes the image's brightness and attempts to apply photometry where it finds intensity peaks to determine if it should be considered a star-like object. The first of these two passes is done on the image minus the sky-map, which was determined in the image preparation, and the second pass is done on the image with the star-like objects identified from the first pass subtracted, to catch any objects that may have been missed due to crowding (Dolphin 2013). To prevent false detections from being made, if two brightness peaks found correspond to only one star-like object, the star-like object is only added to the star list once. The second pass also only locates star-like objects that have brightness peaks in the original and subtracted frames to avoid incorrect detections of objects in the wings of bright stars. And finally, any two star-like objects found to be within 1.5 pixels of each other are combined into a single object on the star list (Dolphin 2013).

Next, the iterative solution is applied, where in this research the number of iterations is set to be just 1. In this stage each star-like object is measured with both the sky-map and all other star-like objects in the image removed, which means that the star-like object being measured is the only object above the detection threshold in the entire image. Once each star-like object on the star list is measured and the iterative solution is finished, DOLPHOT will attempt to determine a residual for the PSFs for each chip and a final solution is made for all the star-like objects (Dolphin 2013).

The properties determined for each star-like object located in each chip are then found in the dolphot output files `chip1.dat` and `chip2.dat`, alongside the corresponding files `chip1.dat.columns` and `chip2.dat.columns` which describe which properties are in each column of the `.dat` files. The properties that this research is concerned with are:

- **Object X Position**: x position in the reference image in pixels.

- **Object Y Position**: y position in the reference image in pixels.
- **Object Type**: The definition of the type of object as defined by DOLPHOT, can either be good star, star too faint for PSF determination, elongated object, object too sharp, or extended object.
- **Instrumental VEGAMAG Magnitude**: Apparent magnitude of the object, in the VEGAMAG system, which takes the Vega star to have a magnitude of 0.
- **Magnitude Uncertainty**: Uncertainty determined by DOLPHOT on the object's intrumental VEGAMAG magnitude.
- **Chi**: The goodness of fit of the PSF to the object,
- **Signal-to-Noise**: S/N, the uncertainty in the total flux from the object.
- **Sharpness**: How much the object differs in structure from the PSF.

Just these property values are then moved to a smaller output file to use for data culling, to remove any objects that DOLPHOT may have included but that are judged to be non-stellar when more strict value cut-offs are applied, and objects too faint to be used for analysis, which ends up being the majority of the DOLPHOT output.

For all target images in this sample all objects with S/N < 5.0, chi > 1.3, absolute value of sharp > 0.1, and any object not identified as a "bright object" are culled out, leaving a list of objects deemed good enough for further analysis. These culling parameters were chosen since they generously include star-like objects while still consistently removing non star-like objects. Figures 2.3, 2.4, and 2.5 below show an example of the number of objects that do and do not meet these requirements in relation to their magnitude for S/N, chi, and sharp for an example target image, for 2MASX J13280261-3145207.

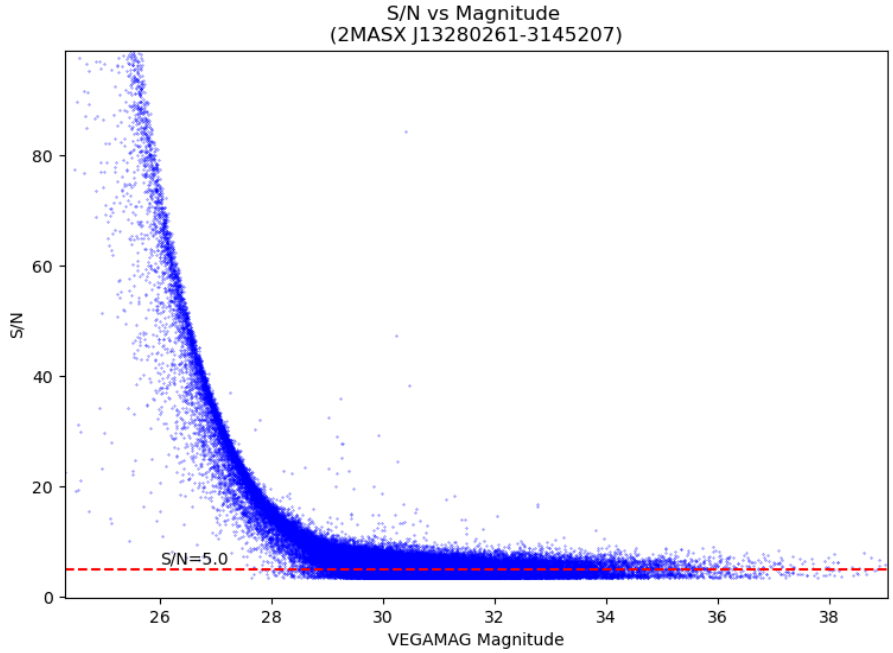

FIGURE 2.3: S/N vs VEGAMAG for 2MASX J13280261-3145207, where objects with a value below 5.0 are culled.

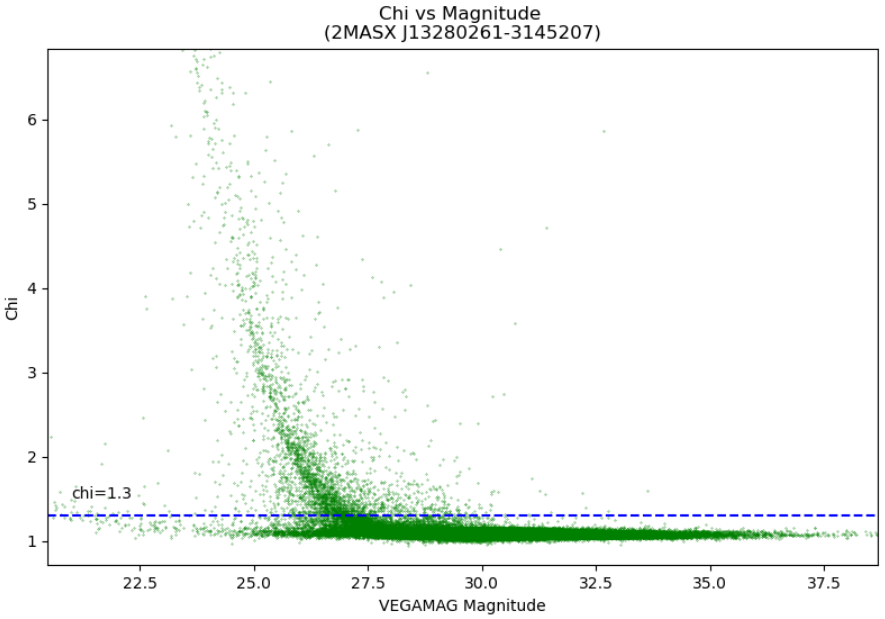

FIGURE 2.4: Chi vs VEGAMAG for 2MASX J13280261-3145207, where objects with a value above 1.3 are culled.

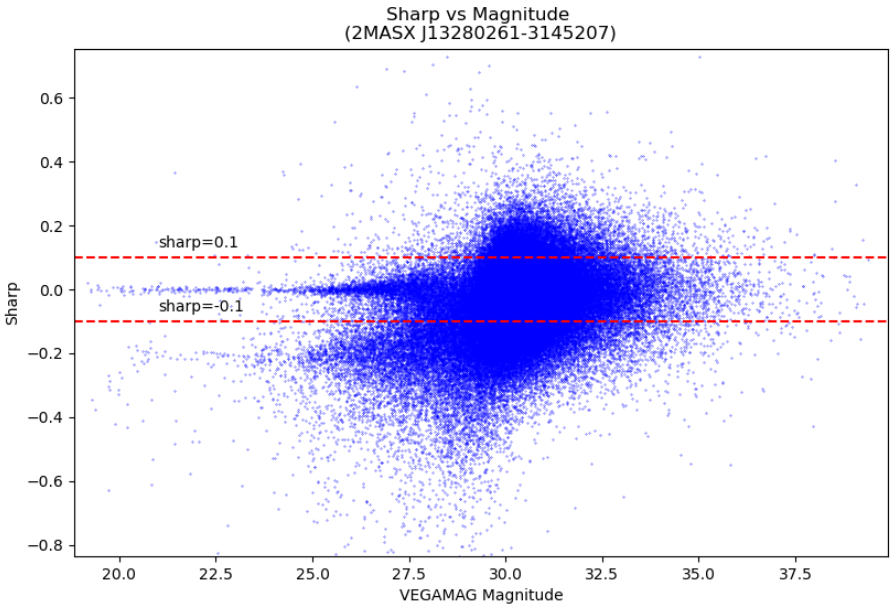

FIGURE 2.5: Sharp vs VEGAMAG for 2MASX J13280261-3145207, where objects with a value above 0.1 or below -0.1 are culled.

2.2.3 Determining Limiting Magnitude

Now that a culled list of star-like objects and their properties for the target image has been obtained, the final properties of the image needs to be determined before moving on to calculating the radial distribution of GCs in the image. Each target image in this sample has a limiting magnitude associated with it, a magnitude at which objects can no longer be reliably detected. In order to determine what this magnitude is, DOLPHOT is simply run again, the same as before, but this time with a list of artificial star-like objects added in to determine how many of them, and at which magnitudes, the routine can identify.

This list of fake star-like objects is generated using a simple python code, where 2500 objects for each chip are created with randomized positions and magnitudes between 19.0 and 40.0, for a total of 5000 fake stars added to the target image. The process is then repeated starting from section 2.2.2, with new parameter files for each of

the chips. These parameter files are identical to those for the original run with the exception of the `FakeStars` and `FakeOut` parameters, which are the name of the input list of artificial star-like objects, and the name of the output data file from this fake star run (similar to `chip1.dat` from the first run). Dolphot is then run again with the same command just with the updated parameter file: `dolphot chip*.dat -pchip*_fake.param > output*_fake.log &` where * is either 1 or 2. Here `chip*.dat` remains the first parameter of the command, as the name of the output file is now defined in the parameter file, and now `chip*.dat` acts as a reference for DOLPHOT to find the correct PSF for the image that was already used in the original run.

The same steps can be applied to the artificial star run output file as was done to the output file from the first run. Once the same key property values are obtained, the same culling criteria can be applied once more. Now the two lists of the artificial star-like objects can be compared; those that are known to be added to the image, and those that the image successfully detected after data culling. Both lists are sorted by magnitude and binned into groups of 0.25 magnitudes, and for each bin the fraction of objects detected is calculated. To ensure no objects are mistaken for one another or counted twice between the lists, two objects are defined as the same if their positions are within 1 pixel of each other.

Once the fraction of detected star-like objects is plotted against magnitude, the relation is fitted by an interpolation function of the form of equation 2.1, where m_o is the magnitude at which 50% of the objects are detected and α is the steepness of falloff as the curve passes through m_o (Harris et al. 2016). For this research the completeness curves of all the images in the sample were fit with $\alpha = 4.3$. Figure 2.6 shows an example, again for 2MASX J13280261-3145207, of how this relation fits to the completeness data.

$$f(m) = \frac{1}{1 + e^{\alpha(m - m_o)}} \tag{2.1}$$

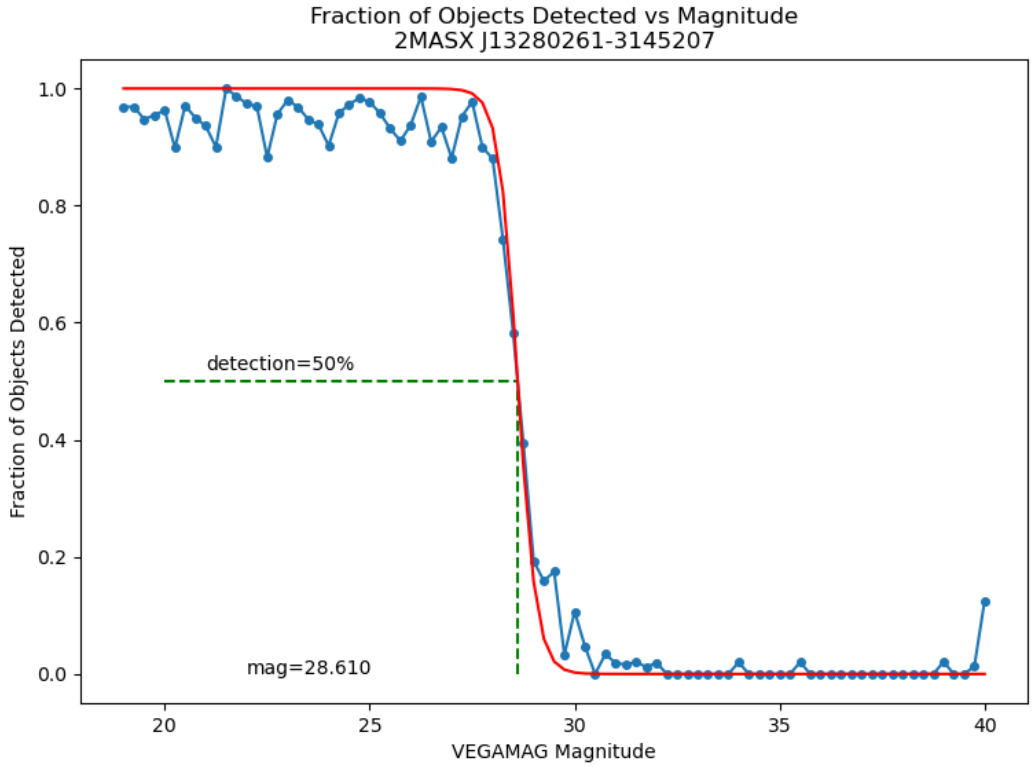

FIGURE 2.6: Fraction of artificial objects detected vs VEGAMAG for 2MASX J13280261-3145207, fit with equation 2.1.

As can be seen in figure 2.6, even at bright magnitudes the completeness never reaches 100%. This is because the positions of the artificial star-like objects were randomly generated, so some will end up too close to the target or satellite galaxies for DOLPHOT to be able to detect, or on top of occasional bright objects already present in the image. However, the limiting magnitude is based on the fit from equation 2.1 and the steepness of the drop-off and thus is not significantly affected by this. With this limiting magnitude determined, the final data culling step is to remove any objects with magnitudes fainter than this limiting magnitude for the image. This is because any objects dimmer than this threshold cannot be reliably detected, and will instead need to be corrected for at a later step, discussed in section 2.3.2.

2.3 GCS Mass

2.3.1 Determining GC Radial Distribution

Now with the culled list of star-like objects in the image and their positions, which we can now refer to as GCs, the distribution of GCs as a function of radial distance from the center of the target galaxy can be calculated. First the image position of the center of the target galaxy must be estimated. This can seem difficult when looking at a reference image, such as figure 2.2, but when the spatial distribution of the culled star-like objects is plotted, like in figure 2.7, it becomes more clear. As one can see, DOLPHOT is able to detect star-like objects in a high-intensity region such as around the target galaxy, but at a certain point will be unable to detect objects when the crowding and intensity is too great. This fact also makes it useful in finding any satellite galaxies that may be significant enough to affect the GC distribution for the target galaxy. This issue is corrected by simply removing an area around these satellite galaxies, but a more sophisticated method is discussed in section 4.2.

In order to determine the area density of GCs as a function of radial distance from the center of the target galaxy, the image is divided into 25 annuli of equal width, as is shown in figure 2.7. The density is then calculated by dividing the number of GCs in each annulus by the number of pixels that are both within the annulus and the image itself, as it can be seen that not all the annuli are entirely within the image. The pixels of any removed satellite galaxies are also removed from the image in order to not count towards the area of the annulus and yield incorrect density values, represented by the blue filled circles in figures 2.7 and 2.8. These annulus areas are converted from pixels to arcseconds squared by simply multiplying the areas by 0.0025, as it is a known property of the ACS camera that the width of each pixel is equivalent to 0.05 arcseconds (Ryon 2019). The radial distance of each of these annuli is also converted to arcseconds in the same way, where the distance is defined as the distance between the center of the

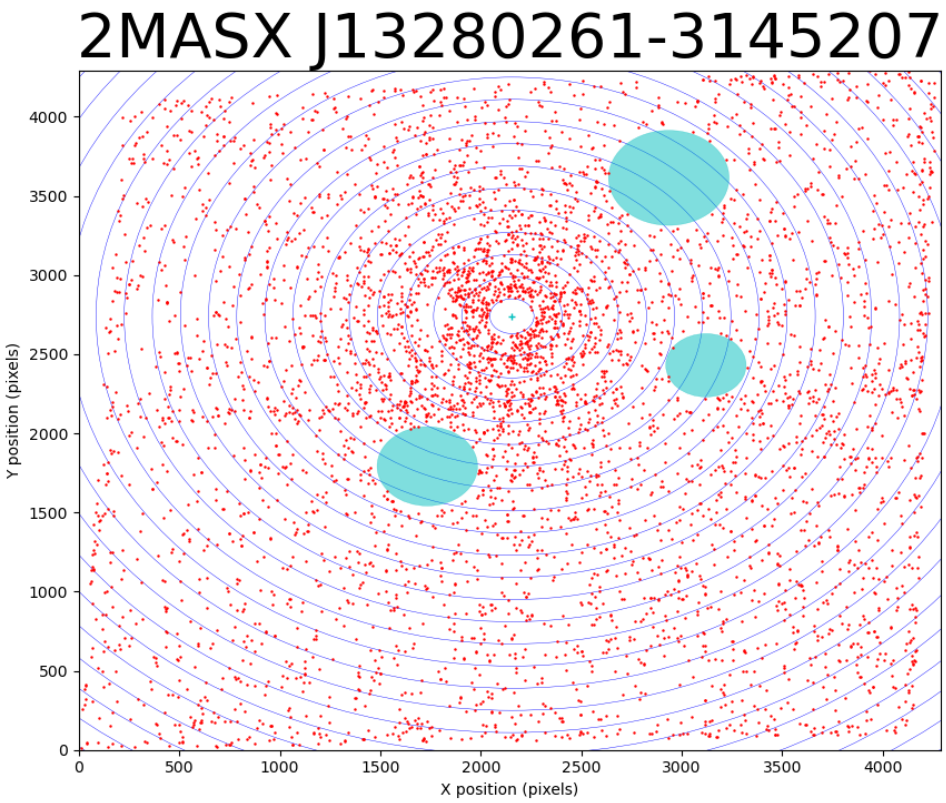

FIGURE 2.7: Spatial distribution of culled data for 2MASX J13280261-3145207, with removed satellite galaxies shown in blue.

target galaxy and the radial midpoint of the annulus. Figure 2.9 shows the relative GC densities of 2MASX J13280261-3145207.

These GC densities, however, have not been corrected for any background densities. The background density of the image is determined from a Hubble Frontier Field (HFF) parallel image that is found to have the closest position in the sky to the target galaxy. The Hubble Frontier Fields refer to images of six deep fields centered on strong lensing galaxy clusters taken with the WFC3 camera, and their parallel counterparts are images of six deep "blank fields" adjacent to these clusters taken with the ACS camera, all of which are available on the HST archive. Due to the fact that all the galaxies in

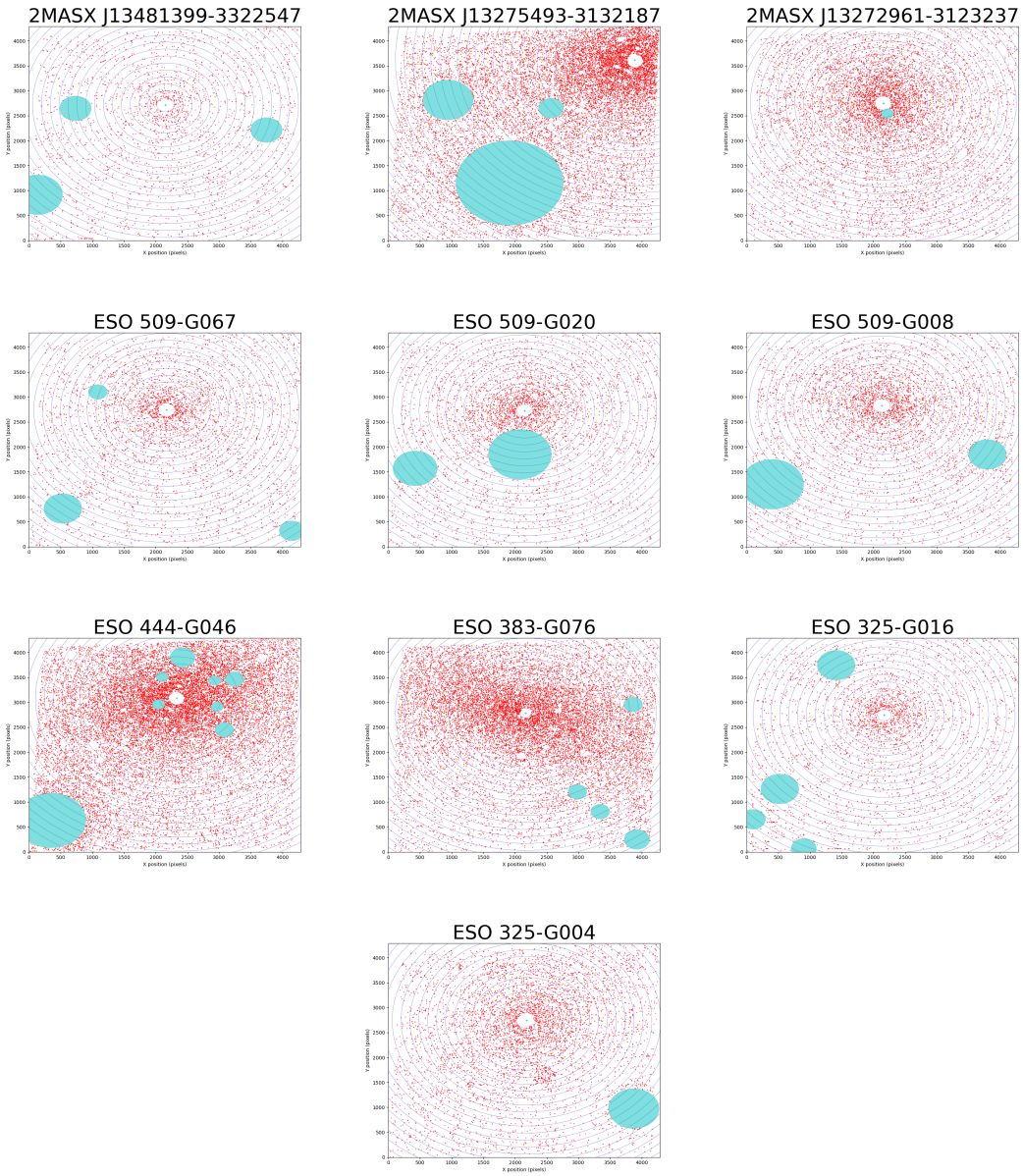

Figure 2.8: Spatial distributions of culled data for all galaxies in the sample, excluding 2MASX J13280261-3145207, which is shown in figure 2.7, with removed satellite galaxies shown in blue.

this sample are relatively close to one another in the sky, the same HFF parallel image can be used for all of them, which happens to be the HFF4 parallel image, located at $l = 230.5°, b = 75.6°$, in the same filter as the sample galaxies; F814W.

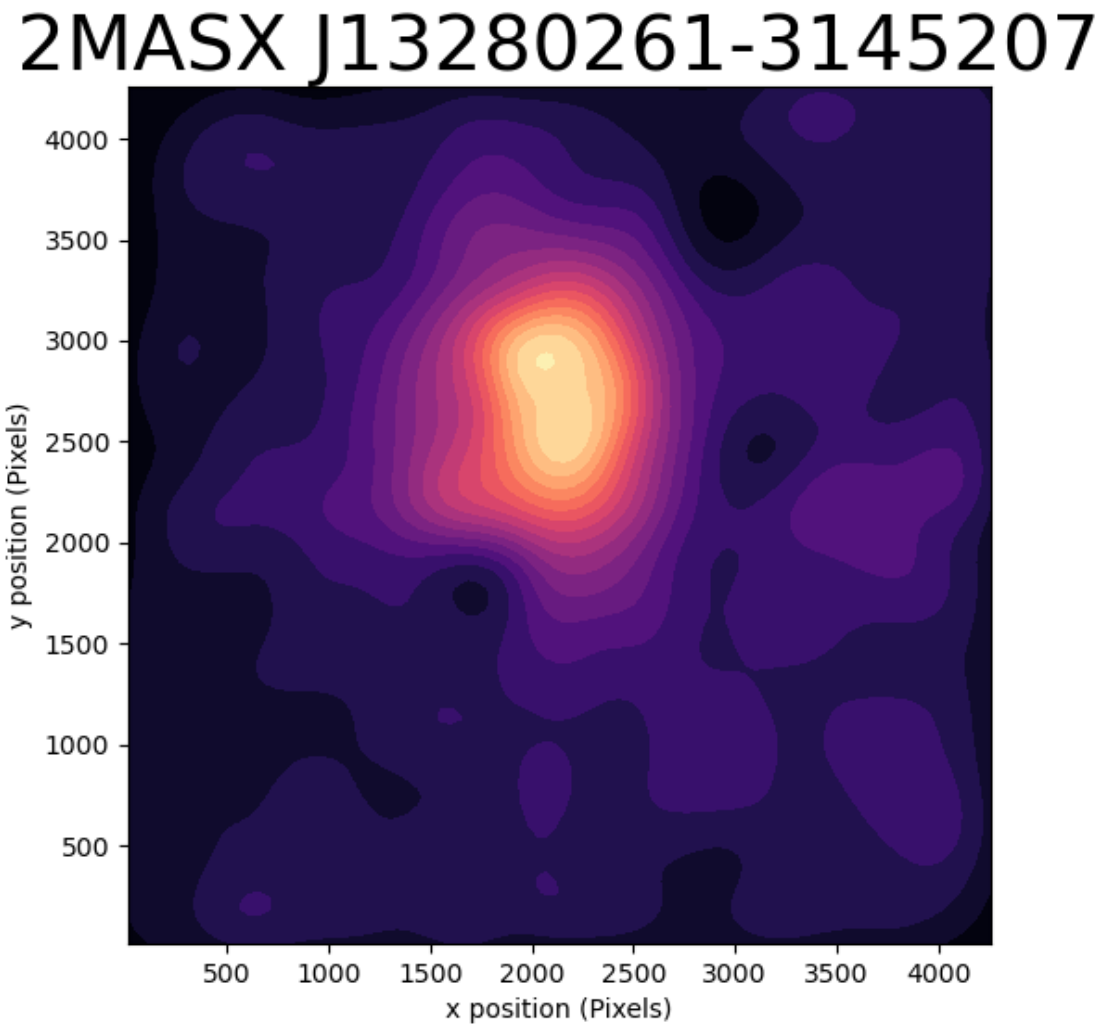

Figure 2.9: Contour map for relative GC densities of star-like objects for MASX J13280261-3145207 after culling.

The combined reference image for HFF4 parallel is then prepared in the exact same way as for the galaxy, and DOLPHOT is then run on it and the data is culled in the same way as well, however the artificial star run does not need to be done, as the limiting magnitude for the target image will be used on HFF4 parallel instead, as the target image is shallower than the HFF4 parallel image. Since there is no target galaxy in the background image, instead of dividing the image into 25 annuli of equal width, the

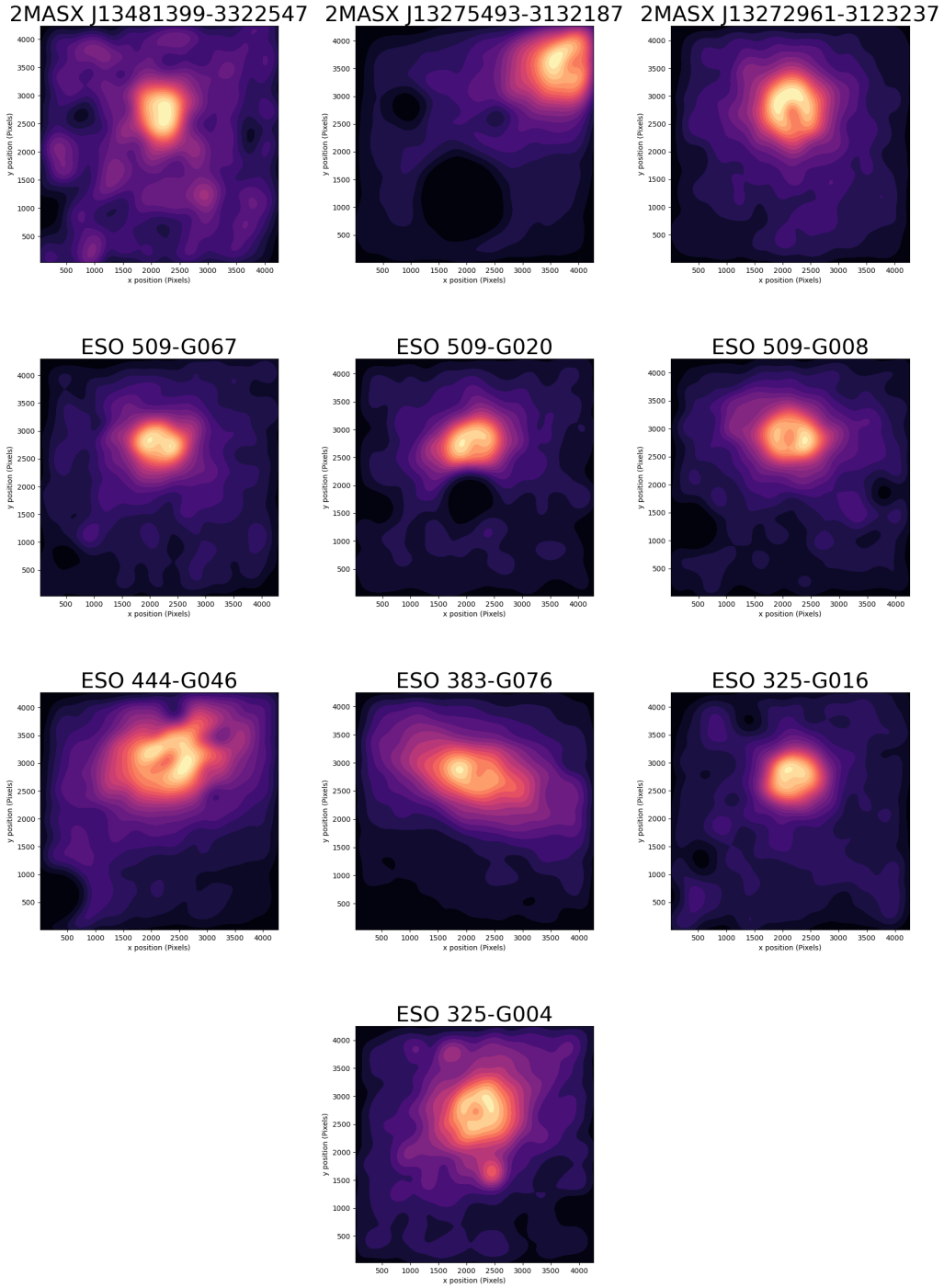

Figure 2.10: Contour map for relative GC densities of star-like objects for all galaxies in the sample after culling, excluding 2MASX J13280261-3145207, which is shown in figure 2.9.

image is divided into a grid of 24 rectangles of equal area instead. The density of star-like, unresolved objects of each of those rectangles is calculated by dividing the number of objects by the area, and those values are averaged to obtain the background object density of the target image and converted to units of objects per arcsecond squared. This is done because although in theory the image is "blank", the scatter of background objects may still not be completely uniform across the entirety of the image, and thus averaging the object density and associated uncertainty over smaller areas rather than globally will result in a more accurate value for the true uncertainty in the background level. This background GC density is then subtracted from every annulus for the target image to yield the true detected radial densities of the galaxy.

This now allows us to plot the GC densities against the radial distance and fit an equation for the GC density distribution for the target galaxy to it. It should be of note that for some of the outermost annuli there are only a handful of GCs within them, and there are very few pixels that fall both in the image and the annulus. Because of this, and that fact that $\sqrt{N}$ Poisson statistics are used here, these annuli may have less accurate densities, and these are shown as the green datapoints in figures 2.11 and 2.12.

This slight inaccuracy can sometimes also occur in the innermost annulus, in this case due to the high intensity at the center of the galaxy. These unreliable datapoints have simply been omitted from figures 2.11 and 2.12, rather than also being highlighted in green. To account for the inability of DOLPHOT to detect GCs at the very center of the target galaxies we assume that the GC density remains constant between the very center and the innermost good annulus, at the density level of the innermost good annulus, which is a reasonable approximation since extrapolating the fit to the centre would be unphysical, the area of that innermost annulus is small, and because observations of galaxies like the Milky Way find that densities do in fact level off in the innermost bulge (Harris and Racine 1979), and this is also seen in M31 (Huxor et al. 2011). Figure 2.12 shows the GC density distribution for 2MASX J13280261-3145207 with a power law fit

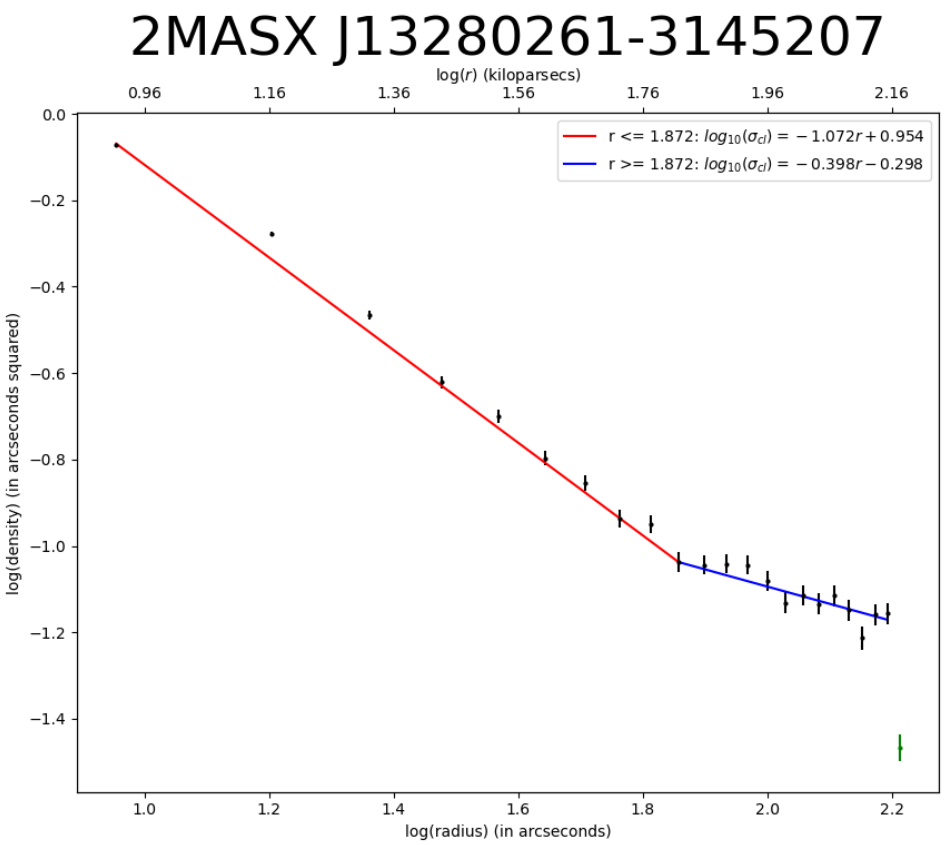

FIGURE 2.11: Piece-wise radial distribution of GC density for 2MASX J13280261-3145207 in log-log space. Green data points represent annuli with not enough pixels in the image and r is in log(arcseconds) for the fit equations.

to the data and 2.11 shows the GC density distribution in log-log space with the same fit.

As can be seen in in figures 2.11 and 2.12, 2MASX J13280261-3145207, as well as several other galaxies in the sample, can be fit with piece-wise functions. In this research, when the outer half of the piece-wise function is seen to be shallower than the inner half, as is most evident in log-log space, this can be interpreted as GCs from the intracluster medium beginning to noticeably influence the GC density distribution. Because all the galaxies in this sample are BCGs this means that at the outer regions,

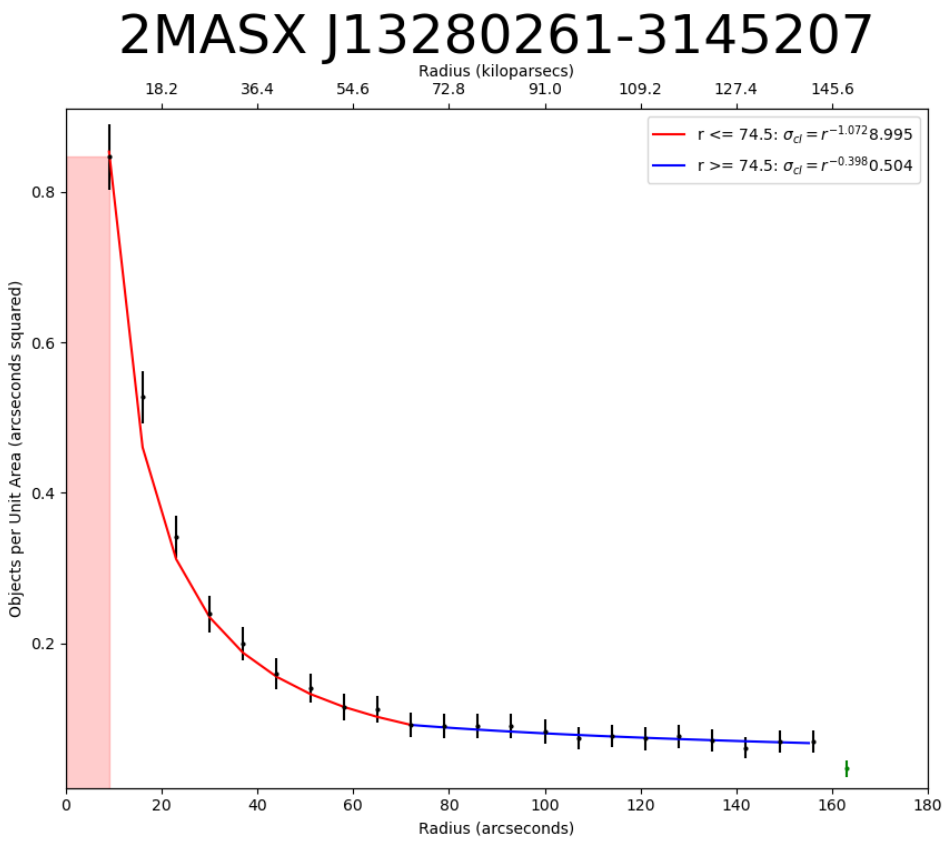

FIGURE 2.12: Piece-wise radial distribution of GC density for 2MASX J13280261-3145207. Green data points represent annuli with not enough pixels in the image and r is in arcseconds here for the fit equations.

GCs from other galaxies in their clusters can be found in the target image, which we do not want to count toward the target galaxy's distribution. Because there is no clear boundary between BCGs and their intracluster medium, these break point radii are used to define a standardization of how far out the GC density distributions are integrated to for each galaxy, discussed in section 2.3.2 below. Table 2.2 presents the limiting magnitudes, the fitting parameters and their associated errors, as well as the integration radius for all the galaxies.

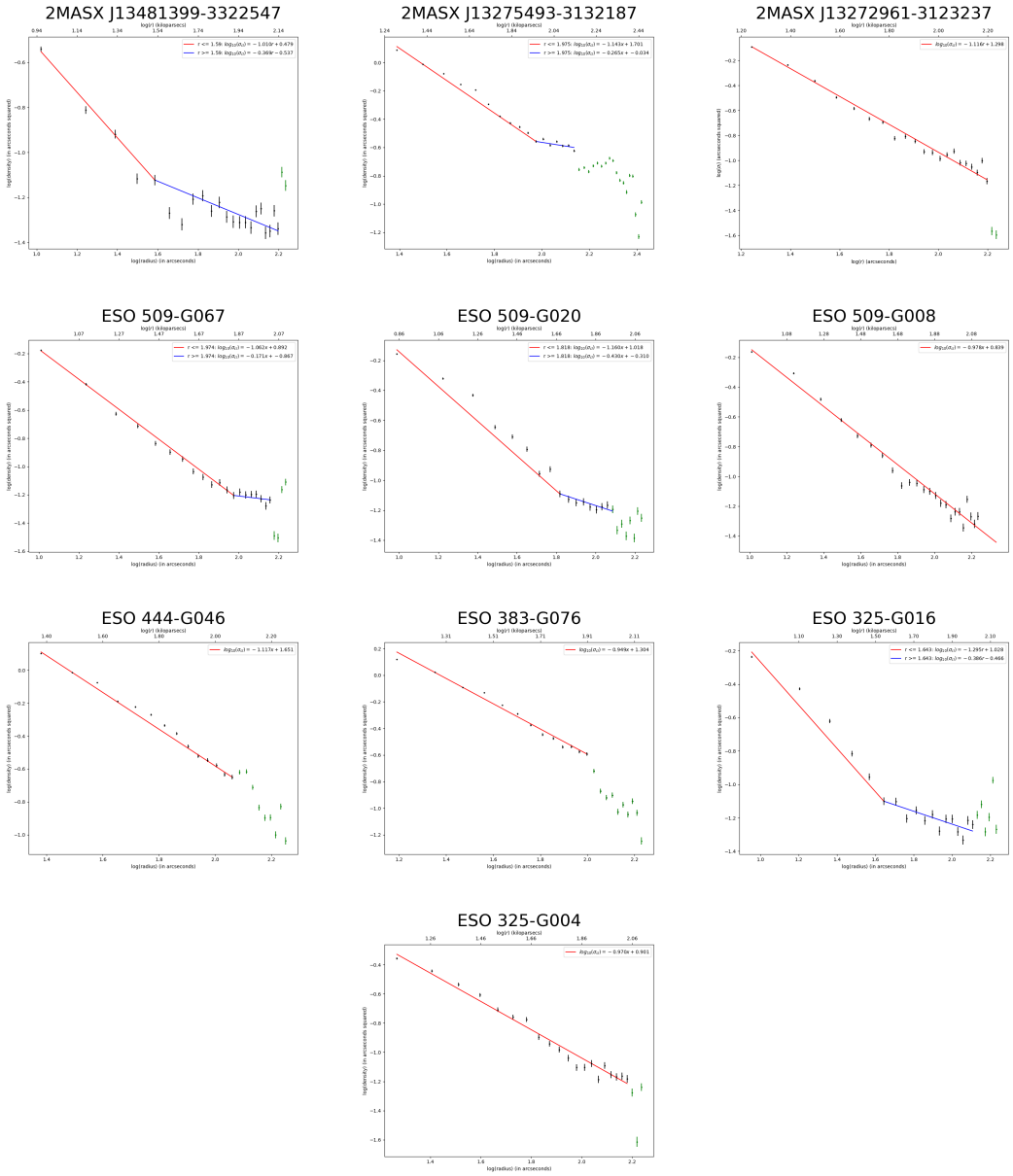

Figure 2.13: Radial distribution of GC density for all galaxies in log-log space, excluding 2MASX J13280261-3145207 which was shown in 2.11. Green data points represent annuli with not enough pixels in the image and r is in log(arcseconds) for the fit equations.

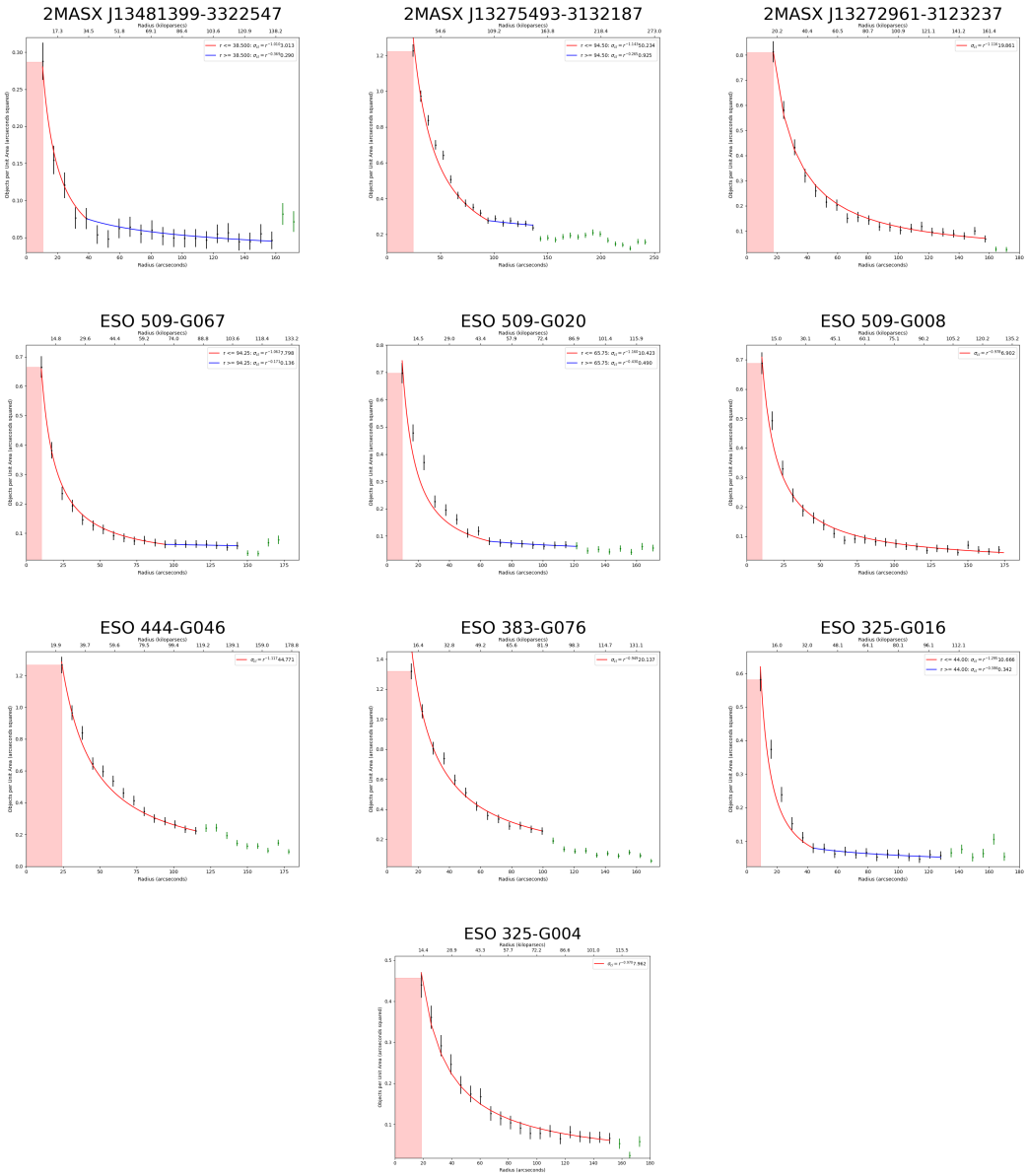

FIGURE 2.14: Radial distribution of GC density for all galaxies, excluding 2MASX J13280261-3145207 which was shown in 2.12. Green data points represent annuli with not enough pixels in the image and r is in arcseconds for the fit equations.

2.3.2 Calculating GCS Mass

Going from the distribution of GC density to a final estimate of the mass of the GCS of a galaxy requires several steps and corrections, the first of which is deciding

Target Name	Area	m	b	m_{lim}	HFF4 σ_{cl}
2MASX J13481399-3322547	Inner	-1.010 ± 0.0180	3.013 ± 0.1978	28.50	2.01×10^{-4}
	Outer	-0.369 ± 0.0153	0.290 ± 0.0162		
2MASX J13281399-3322547	Inner	-1.072 ± 0.0016	8.991 ± 0.0631	28.61	2.22×10^{-4}
	Outer	-0.398 ± 0.0319	0.504 ± 0.0688		
2MASX J13275493-3132187	Inner	-1.143 ± 0.0003	50.234 ± 0.0651	28.40	1.82×10^{-4}
	Outer	-0.265 ± 0.0321	0.925 ± 0.1350		
2MASX J13272961-3123237	All	-1.116 ± 0.0069	19.861 ± 0.4348	28.47	1.95×10^{-4}
ESO 509-G067	Inner	-1.062 ± 0.0035	7.798 ± 0.1237	28.29	1.64×10^{-4}
	Outer	-0.171 ± 0.0797	0.136 ± 0.0493		
ESO 509-G020	Inner	-1.160 ± 0.0036	10.423 ± 0.1559	28.17	1.47×10^{-4}
	Outer	-0.430 ± 0.0480	0.490 ± 0.0985		
ESO 509-G008	All	-0.978 ± 0.0063	6.902 ± 0.1354	28.20	1.52×10^{-4}
ESO 444-G046	All	-1.117 ± 0.0005	44.771 ± 0.0995	28.45	1.90×10^{-4}
ESO 383-G076	All	-0.949 ± 0.0007	20.137 ± 0.0675	28.19	1.49×10^{-4}
ESO 325-G016	Inner	-1.295 ± 0.0066	10.666 ± 0.2648	28.24	1.57×10^{-4}
	Outer	-0.386 ± 0.0234	0.342 ± 0.0302		
ESO 325-G004	All	-0.970 ± 0.0117	7.962 ± 0.3552	28.09	1.34×10^{-4}

Table 2.2: List of target galaxies with fitting parameters for their σ_{cl} fits for both the radii before and after their breakpoint radius, or for the whole fit for those that are not piecewise (of the form $\sigma_{cl} = r^m b$). The limiting magnitudes and the background densities (in objects per arcseconds squared) are also included.

how far out to integrate the σ_{cl} expression. There are two methods of standardization done for this research, one based on the half-light radii of the galaxies (R_e), and the other based on the virial radii of the galaxies (R_{vir}). In order to determine how far out to integrate the GC radial distribution to include the entire GCS without allowing significant interference from the inter-cluster medium GCs using R_e, we begin by using the piece-wise distributions of galaxies that are assumed to be influenced by GCs from the intergalactic medium. The break-point radii in these galaxies' distributions are assumed to be the size of the galaxies' GCSs, as the shallower distribution would imply extra GCs not associated with the galaxy are being detected. This radius is then divided by the galaxy's R_e and those values are averaged to yield a factor, which when multiplied by R_e, will give the standardized radius to integrate σ_{cl} out to for all galaxies in the sample, which in this case was 5.53. The half-light radii of the ESO galaxies in the sample are available on the NED database, but only the isophotal diameters (D_{25}) of the four 2MASX galaxies were available, so these radii were converted assuming the

difference between $\log(R_{25})$ and $\log(R_e)$ was relatively constant, defined as Δ_R. These Δ_R values were found for all the ESO galaxies in the sample as well as for UGC 9799 and UGC 10143, which are BCGs of similar size to the galaxies in the sample, and then these values were averaged and applied to the 2MASX galaxies with unknown half-light radii. $\Delta_R = 0.69 \pm 0.11$ was used to find these half-light radii.

The method of standardization using R_{vir} however, does not rely on both determining the location of the breakpoint radii and making the assumption that it corresponds to where the inter-cluster medium's influence begins. Instead, all galaxies are integrated out to $0.1R_{vir}$, which as shown in table 2.3, is very similar in size to $5.53R_e$ for most of the galaxies in the sample. The virial radii were calculated using equation 2.2, assuming that the virial masses and the halo masses for these galaxies were similar enough to be assumed the same, and using $H_o = 70km/s/Mpc$

$$\begin{aligned} M_{vir} &= \left(\frac{4}{3}\pi R_{vir}^3\right)(200\rho_c) \\ M_{vir} &= \left(\frac{4}{3}\pi R_{vir}^3\right)200\frac{3H_o^2}{8\pi G} \\ R_{vir} &= \left[\frac{GM_{vir}}{100H_o^2}\right]^{1/3} \\ &= 20.61pc\left(\frac{M_{vir}}{M_\odot}\right)^{1/3} \end{aligned} \tag{2.2}$$

For most of the sample these radii will be well within the image, but for the two most massive galaxies, this will actually go out past the bounds of the image, and for a few of the galaxies in the sample these standardized radii will also go past their piecewise break-point. For both of these standardization techniques, $N_{GC} = \int \sigma_{cl} 2\pi r dr$ will yield a first estimate for the number of GCs in the galaxy (N_{GC}), with an error derived from the uncertainty on the fit values in the σ_{cl} expression.

The next step is to correct the N_{GC} estimate in order to account for the GCs that

Target Name	$R_e(pc)$	$R_{vir}(pc)$	$5.53R_e(pc)$	$0.1R_{vir}(pc)$
2MASX J13481399-3322547	9.86×10^3	5.53×10^5	5.46×10^4	5.53×10^4
2MASX J13280261-3145207	9.72×10^3	4.93×10^5	5.38×10^4	4.93×10^4
2MASX J13275493-3132187	1.58×10^4	7.81×10^5	8.76×10^4	7.81×10^4
2MASX J13272961-3123237	6.62×10^3	8.56×10^5	3.67×10^4	8.56×10^4
ESO 509-G067	1.22×10^4	6.67×10^5	6.78×10^4	6.67×10^4
ESO 509-G020	8.37×10^3	6.83×10^5	4.63×10^4	6.83×10^4
ESO 509-G008	1.12×10^4	7.85×10^5	6.21×10^4	7.85×10^4
ESO 444-G046	3.28×10^4	1.41×10^6	1.82×10^5	1.41×10^5
ESO 383-G076	7.54×10^4	1.24×10^6	4.17×10^5	1.24×10^5
ESO 325-G016	5.40×10^3	5.41×10^5	2.99×10^4	5.41×10^4
ESO 325-G004	1.20×10^4	8.54×10^5	6.62×10^4	8.54×10^4

Table 2.3: List of target galaxies with half-light radii, virial radii, and the integration radii calculated from those radii.

are below the limiting magnitude of the image. First, the distance modulus, $(m - M)_I$, for the galaxy is calculated from its velocity and Hubble distance, both found on the NASA/IPAC Extragalactic Database (NED), and is used to convert the limiting magnitude from apparent to absolute. Then, we compare the absolute limiting magnitude to the peak magnitude for the GC Luminosity function, which is found to be located at $M_I = -9.0$ (Harris et al. 2014). For large galaxies, such as the ones in this sample, the Gaussian function has a sigma of $\sigma_g = 1.30$ magnitudes (Harris et al. 2014). Dividing the difference between the peak and the limiting magnitude by σ_g, gives the number of standard deviations dimmer the image's photometric limit is than the GCLF peak. That number of standard deviations can then simply be converted to the fraction of the total population included in the original estimate. We can then divide the first N_{GC} estimate by that fraction to obtain the final, corrected, total N_{GC} estimate for the galaxy.

Next, to convert the number of GCs in the galaxy to the mass of the GCS, we can make this estimate quite easily by just multiplying this value by the average individual GC mass in the galaxy. This average GC mass can be calculated from the total visual magnitude of the galaxy (M_V^T), which can also be found on NED, using equation 2.3 (Harris et al. 2017). Finally, multiplying total N_{GC} by $\langle M_{GC} \rangle$ gives the final total GCS

mass, M_{GCS}.

$$\log\langle M_{GC}\rangle = 5.698 + 0.1294 M_V^T + 0.0054 (M_V^T)^2 \tag{2.3}$$

2.3.3 Example of M_{GCS} Calculation for 2MASX J13280261-3145207

In this subsection I will go through each step of the M_{GCS} calculation process for the galaxy 2MASX J13280261-3145207 as an example, which can be applied to the rest of the sample. First, the preliminary estimate of the number of GCs in the system needs to be determined from the integration of σ_{cl}, taking into account the assumptions made for the area between the innermost annulus and the center of the galaxy, as well as the errors on the fit parameters for σ_{cl}. This example is done using the R_e standardization, which is to integrate out to $5.536R_e$, which for this galaxy is 62.1", which is before the breakpoint radius.

$$\begin{aligned} N_{GC} &= \int_{0"}^{9.0"} (0.844 \pm 0.0430)(2\pi r) dr + \int_{9.0"}^{62.1"} r^{(-1.072 \pm 0.0016)} (8.995 \pm 0.0631)(2\pi r) dr \\ &= (214.77 \pm 10.95) + (2341.54 \pm 16.81) \\ &= 2556.31 \pm 27.76 \end{aligned} \tag{2.4}$$

Now the absolute limiting magnitude of the galaxy is calculated from its apparent limiting magnitude and the galaxy's distance modulus in the F814W filter, which is shown in table 2.1.

$$\begin{aligned} M_{lim} &= m_{lim} - (m - M)_I \\ &= 28.61 - (36.446 \pm 0.0045) \\ &= -7.836 \pm 0.0045 \end{aligned} \tag{2.5}$$

Next, this limiting magnitude is compared to the peak of the GCLF, and divided by the σ_g of the Gaussian function associated with the galaxy. This gives the number of standard deviations dimmer the galaxy's limiting magnitude is than the GCLF peak.

$$\begin{aligned}\frac{M_{peak} - M_{lim}}{\sigma_g} &= \frac{(-9.0 \pm 0.1) - (-7.836 \pm 0.0045)}{1.30 \pm 0.1} \\ &= -1.069 \pm 0.1033 \end{aligned} \tag{2.6}$$

This number can be looked up in a standard Gaussian function table of data to determine what fraction of the total GC population is below the limiting magnitude (f_{lim}), and divide it by our original number estimate to get the total one.

$$\begin{aligned}N_{GC,tot} &= \frac{N_{GC}}{f_{lim}} \\ &= \frac{2556.31 \pm 27.76}{0.8554 \pm 0.0196} \\ &= 2988.44 \pm 55.45 \end{aligned} \tag{2.7}$$

Now, the average mass of a GC in the galaxy can be determined from equation 2.3 using the galaxy's total visual magnitude, shown in table 2.1.

$$\begin{aligned}\log\langle M_{GC}\rangle &= 5.698 + 0.1294 M_V^T + 0.0054 (M_V^T)^2 \\ \log\langle M_{GC}\rangle &= 5.698 + 0.1294(-22.00) + 0.0054(-22.00)^2 \\ \log\langle M_{GC}\rangle &= 5.698 - 2.8468 + 2.6136 \\ \langle M_{GC}\rangle &= 10^{5.4648} \\ \langle M_{GC}\rangle &= 2.92 \times 10^5 M_\odot \end{aligned} \tag{2.8}$$

Finally, the M_{GCS} for 2MASX J13280261-3145207 is easily found by multiplying the total number of GCs by the average GC mass for the galaxy.

$$\begin{aligned} M_{GCS} &= N_{GC,tot}\langle M_{GC}\rangle \\ &= (2988.44 \pm 55.45)(2.92 \times 10^5 M_\odot) \\ &= (8.71 \pm 0.162) \times 10^8 M_\odot \end{aligned} \tag{2.9}$$

2.4 Dark Matter Halo Mass

Compared to the process of determining GCS mass, determining the dark matter halo mass (M_h) of a galaxy is much less involved. This mass is determined from just the total stellar mass of the galaxy. In order to obtain the total stellar mass, we must begin with finding the total K-band magnitude, (M_K). This can easily be found from determining the K-band distance modulus with the galaxy's Hubble distance and K-band extinction found on NED, and its total K-band apparent magnitude from the 2 Micron All Sky Survey (2MASS) database. These K-band magnitudes and extinctions, as well as the CMB velocities and Hubble distances ($H_o = 70km/s/Mpc$) of the sample galaxies are shown in table 2.4. From the M_K value, The galaxy's total luminosity in the K-band (L_K) value can be calculated assuming $M_{K,\odot} = 3.32$, and using equation 2.10 (Bell et al. 2003).

$$\log(L_k/L_\odot) = \frac{M_{K,\odot} - M_K}{2.5} \tag{2.10}$$

Next, the total stellar mass can be found using the K-band stellar mass-to-light ratio shown in equation 2.11 (Bell et al. 2003). Here $(B-V)_o$ is the galaxy's intrinsic integrated colour, which is taken to be 0.95 for massive galaxies like those in this sample

Target Name	m_K	A_K	$V(km/s)$	$D(Mpc)$
2MASX J13481399-3322547	10.787 ± 0.048	0.016	12468 ± 19	178.114 ± 0.271
2MASX J13280261-3145207	11.112 ± 0.061	0.016	13140 ± 27	187.714 ± 0.386
2MASX J13275493-3132187	10.686 ± 0.054	0.015	15765 ± 28	225.214 ± 0.400
2MASX J13272961-3123237	10.372 ± 0.052	0.018	14565 ± 25	208.071 ± 0.357
ESO 509-G067	10.143 ± 0.042	0.020	10683 ± 45	152.614 ± 0.643
ESO 509-G020	10.037 ± 0.036	0.017	10456 ± 35	149.370 ± 0.500
ESO 509-G008	9.872 ± 0.034	0.016	10848 ± 21	154.970 ± 0.300
ESO 444-G046	9.494 ± 0.052	0.015	14345 ± 29	204.930 ± 0.414
ESO 383-G076	9.313 ± 0.037	0.016	11832 ± 21	169.030 ± 0.300
ESO 325-G016	10.705 ± 0.042	0.024	11564 ± 19	165.200 ± 0.270
ESO 325-G004	9.654 ± 0.035	0.018	10420 ± 20	148.860 ± 0.286

TABLE 2.4: List of target galaxies with apparent magnitude in the K-band, galactic extinction in the K-band, CMB velocity, and Hubble distance ($H_o = 70km/s/Mpc$).

(Gallagher et al. 1980). The total stellar mass can also be calculated using the mass-to-light ratio in the V band, but the K band magnitudes are more readily available in the (2MASS) database for the galaxies in my sample, and also because it has been found that using K band luminosity results in a better stellar mass estimate (Bell et al. 2003).

$$\log(M_\star/L_K) = -0.356 + 0.135(B-V)_o \tag{2.11}$$

Finally, the galaxy's M_h can be calculated using equation 2.12, where $M_1 = 10^{10.76} M_\odot$, defined as the pivot mass (Hudson et al. 2015).

$$M_\star/M_h = 0.0454 \left[\left(\frac{M_\star}{M_1} \right)^{-0.43} + \frac{M_\star}{M_1} \right]^{-1} \tag{2.12}$$

2.4.1 Example of M_h Calculation for 2MASX J13280261-3145207

As was done in section 2.3.3, this section will go through the calculation of the dark matter halo mass for 2MASX J13280261-3145207. First, the distance modulus in the K-band is calculated, and that combined with the apparent magnitude in the K-band

will yield the absolute magnitude in the K-band.

$$\begin{aligned} m_K - M_K &= 2.5\log([d/10]^2) + A_K \\ m_K - M_K &= 2.5\log([(187.714 \pm 0.386) \times 10^5]^2) + 0.016 \\ m_K - M_K &= 36.607 \pm 0.00373 \\ M_K &= (10.372 \pm 0.052) - (36.607 \pm 0.00373) \\ M_K &= -26.235 \pm 0.05573 \end{aligned} \tag{2.13}$$

Next, equation 2.10 is used to take this absolute magnitude and change it to luminosity in the K-band.

$$\begin{aligned} \log(L_k/L_\odot) &= \frac{M_{K,\odot} - M_K}{2.5} \\ \log(L_k/L_\odot) &= \frac{3.32 - (-26.235 \pm 0.05573)}{2.5} \\ L_K/L_\odot &= 10^{11.822 \pm 0.02229} \\ L_K &= (6.637 \pm 0.341) \times 10^{11} L_\odot \end{aligned} \tag{2.14}$$

This luminosity can then be used with equation 2.11 to obtain the total stellar mass of 2MASX J13280261-3145207, taking $(B-V)_o$ to be 0.95 for BCGs such as this.

$$\begin{aligned} \log(M_\star/L_K) &= -0.356 + 0.135(B-V)_o \\ \log(M_\star/L_K) &= -0.356 + 0.135(0.95) \\ M_\star &= (6.637 \pm 0.341) \times 10^{11} L_\odot (10^{-0.22775}) \frac{M_\odot}{L_\odot} \\ M_\star &= (3.928 \pm 0.202) \times 10^{11} M_\odot \end{aligned} \tag{2.15}$$

Finally, using equation 2.12 this stellar mass can be converted to the final dark matter halo mass for MASX J13280261-3145207.

$$
\begin{aligned}
M_\star/M_h &= 0.0454\left[\left(\frac{M_\star}{M_1}\right)^{-0.43} + \frac{M_\star}{M_1}\right]^{-1} \\
M_h &= \frac{M_\star}{0.0454}\left[\left(\frac{M_\star}{10^{10.76}M_\odot}\right)^{-0.43} + \frac{M_\star}{10^{10.76}M_\odot}\right] \\
M_h &= (8.652 \pm 0.445) \times 10^{12} M_\odot \left[(0.438 \pm 0.010) + (6.826 \pm 0.351)\right] \\
M_h &= (6.285 \pm 0.450) \times 10^{13} M_\odot
\end{aligned} \tag{2.16}
$$

Chapter 3

Results

This chapter will summarize the results of this research and discuss how it compares to the literature on the $M_{GCS} - M_h$ relation, both previous observational and theoretical works. The GC system and dark matter halo masses for the galaxies in the sample will be summarized, they will be shown plotted against each other in log-log space. The η value will be determined for this sample, as well for this sample added to a literature catalogue of galaxies to determine what change these results have on the overall relation shape and steepness.

3.1 Mass Results

Following the methodology laid out in sections 2.3.3 and 2.4.1, the masses for the galaxies in the sample were determined, where M_{GCS} was determined twice through two methods adopting different ways to standardize the outer radial limit for calculating the total GC population; once using the half light radius, and once using the virial radius. These masses are shown in table 3.1, and it should be noted that $5.53R_e$ encloses approximately 89.95% of the total light in a given galaxy, by De Vaucouleur's Law. Comparatively, the average amount of light enclosed by $0.1R_{vir}$ for the galaxies in this research sample is 92.20%, although that percentage varies from galaxy to galaxy as there is no simple conversion between R_e and R_{vir}. These GCS masses were then plotted

against the dark matter halo masses in log-log space and a linear fit was determined from the galaxy sample, in turn providing an estimate for η. These plots are shown in figures 3.1 and 3.2 yielding $\eta = (7.33 \pm 0.26_{internal} \pm 1.47_{external}) \times 10^{-5}$ and $\eta = (6.84 \pm 0.10_{internal} \pm 1.37_{external}) \times 10^{-5}$, respectively. Here the internal uncertainty is the uncertainty associated with the weighted fit to the data points, and the external uncertainty is the systematic uncertainty on the $M_\star - M_h$ relation. The shaded regions of the figures represents the systematic uncertainty caused by the uncertainty in the $M_\star - M_h$ relation, found by Coupon et al. (2015) to be $\sim 0.2dex$ for galaxies in the mass range of this research's sample.

Target Name	N_{GC}		$M_{GCS}(\times 10^9 M_\odot)$		$M_h(\times 10^{14} M_\odot)$
	$5.53R_e$	$0.1R_{vir}$	$5.53R_e$	$0.1R_{vir}$	
J13481399-3322547	1555 ± 77	1688 ± 85	0.42 ± 0.06	0.46 ± 0.06	0.19 ± 0.04
J13280261-3145207	2988 ± 55	2620 ± 169	0.87 ± 0.02	0.76 ± 0.05	0.14 ± 0.03
J13275493-3132187	18592 ± 402	29529 ± 632	7.66 ± 0.17	12.17 ± 0.26	0.54 ± 0.12
J13272961-3123237	3279 ± 88	16023 ± 340	1.35 ± 0.04	6.60 ± 0.14	0.72 ± 0.16
ESO 509-G067	4045 ± 104	3940 ± 101	1.67 ± 0.06	1.62 ± 0.06	0.34 ± 0.09
ESO 509-G020	2672 ± 65	4068 ± 258	0.90 ± 0.03	1.37 ± 0.09	0.36 ± 0.06
ESO 509-G008	4441 ± 112	5675 ± 143	1.38 ± 0.04	1.76 ± 0.05	0.55 ± 0.12
ESO 444-G046	39131 ± 830	30566 ± 644	60.01 ± 1.27	46.88 ± 0.99	3.20 ± 0.74
ESO 383-G076	107452 ± 2417	28474 ± 645	58.27 ± 2.70	15.44 ± 0.72	2.15 ± 0.47
ESO 325-G016	1172 ± 32	2014 ± 82	0.37 ± 0.01	0.64 ± 0.03	0.18 ± 0.04
ESO 325-G004	5705 ± 217	7670 ± 290	2.32 ± 0.09	3.11 ± 0.12	0.71 ± 0.16

TABLE 3.1: List of target galaxies with calculated N_{GC} and M_{GCS} with integration radius determined from both the half-light radius and the virial radius, and M_h.

The next step to analyze the relationship between these masses is to plot them against each other alongside datapoints from galaxies of a wider range of masses to see how this new sample of high-mass galaxies will affect the overall $M_{GCS} - M_h$ relation. These lower mass galaxies consist of a subset of 303 galaxies taken from the Harris et al. (2013) catalogue, and have halo masses ranging from $10^{10} - 10^{14} M_\odot$. Figures 3.3 and 3.4 again show M_{GCs} determined from R_e and R_{vir} plotted against M_h, this time for the full range of masses. It should be noted here that the systematic uncertainty is not applied due to the fact that the halo masses of the catalogue of galaxies were calculated using varying methods, thus the uncertainty associated with the method used in this

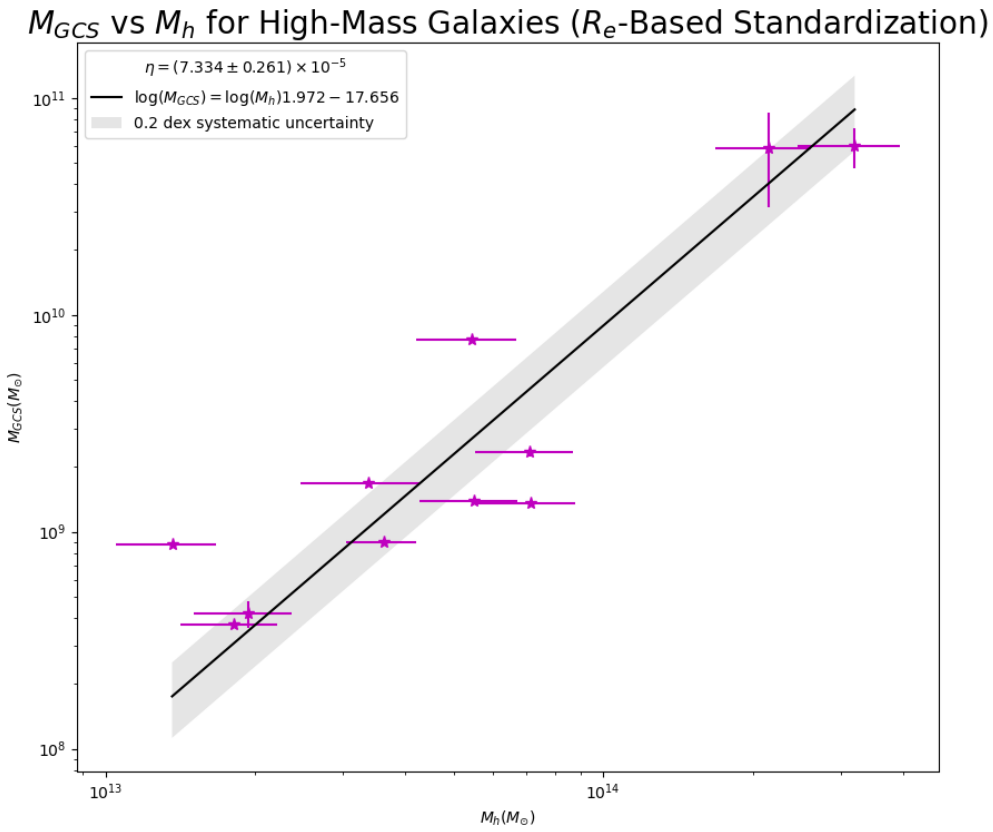

FIGURE 3.1: M_{GCS} determined from R_e standardization plotted against M_h for the galaxies in the sample in log-log space. Systematic uncertainty comes from the $M_\star - M_h$ relation.

research could not be applied globally. As expected, the η values vary much less between the R_e-based and the R_{vir}-based data than for the η-values taken from only the galaxies in the high-mass sample, with $\eta = (2.96 \pm 0.13) \times 10^{-5}$ and $\eta = (2.99 \pm 0.06) \times 10^{-5}$, respectively. These values are both, however, higher than the η-value from the lower-mass catalogue galaxies alone, found to be $\eta = (2.87 \pm 0.11) \times 10^{-5}$. This shows that although the sample of galaxies used in this research is comparatively much smaller than the catalogue of galaxies it is being compared to, it has a not-insignificant effect on the slope of the $M_{GCS} - M_h$ relation as a whole, and by extension η.

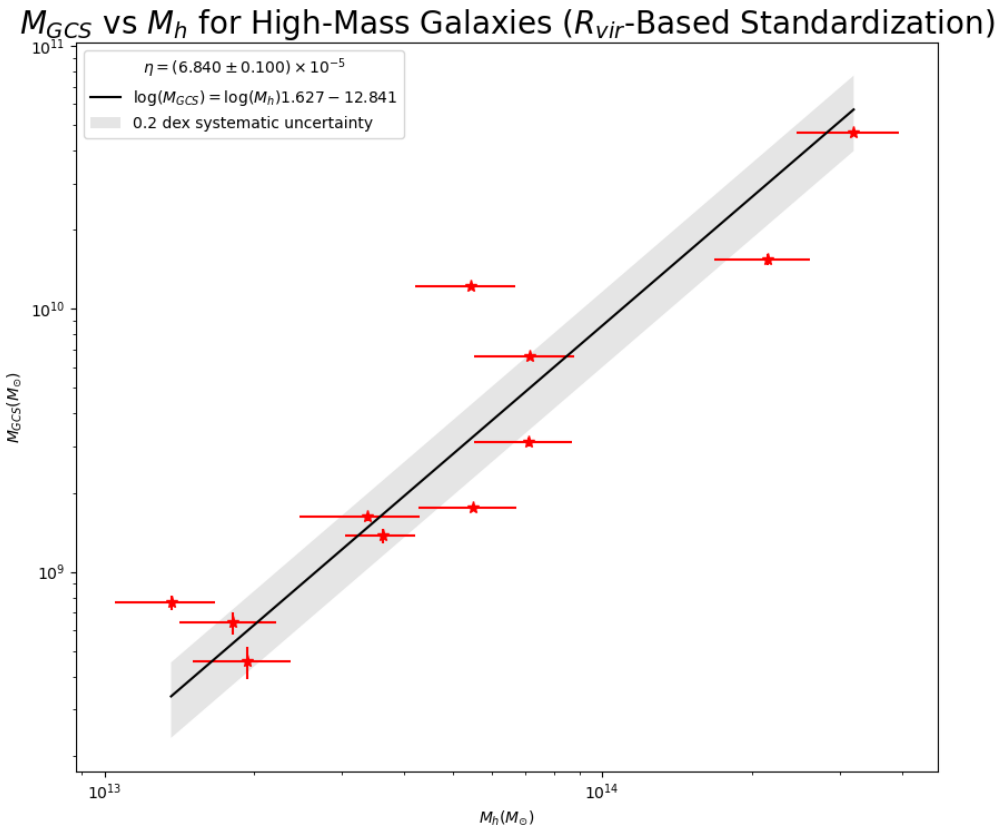

FIGURE 3.2: M_{GCS} determined from R_{vir} standardization plotted against M_h for the galaxies in the sample in log-log space. Systematic uncertainty comes from the $M_\star - M_h$ relation.

3.1.1 Comparing R_e vs R_{vir} Standardization Methods

One of the goals of this research was to propose a new, standardized method of determining the size of the GCS, especially for BCGs, which can have GCs within their inter-cluster medium not associated with their GCS, but rather that of their satellite galaxies. With a lack of a clear definition of where to place the GCS boundary for these massive galaxies, it is difficult to reliably compare N_{GCS} and M_{GCS} for galaxies calculated by different research groups. This is seen even here, in figures 3.3 and 3.4, as we see the catalogue galaxies with halo masses greater than $10^{14} M_\odot$ have M_{GCS} lower

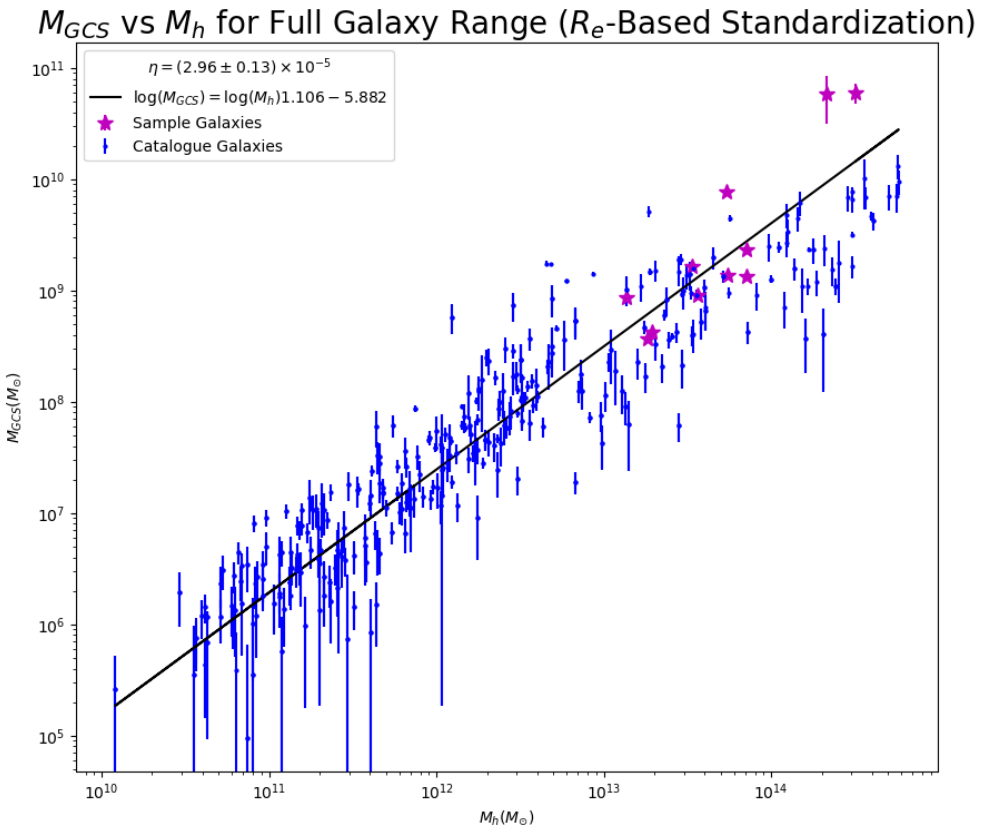

FIGURE 3.3: M_{GCS} determined from R_e standardization plotted against M_h for the galaxies in the sample (red stars) and for the galaxies in literature catalogues (Harris et al. 2013) (blue points) in log-log space.

than we would expect from both the linear fit and the masses of the galaxies in this research's sample. Without standardizing the size of the GCS it is difficult to properly compare the sample and catalogue high-mass galaxies.

In order to combat this issue, two definitions of GCS size are proposed here, one based on galaxy R_e, and the other on galaxy R_{vir}. How these definitions were determined is discussed in chapter 2, section 2.3.2, and here the results that both definitions yielded will be compared. First, when comparing both the η-values calculated from the sample of galaxies alone, and when added to the catalogue of galaxies, the R_{vir}-based definition

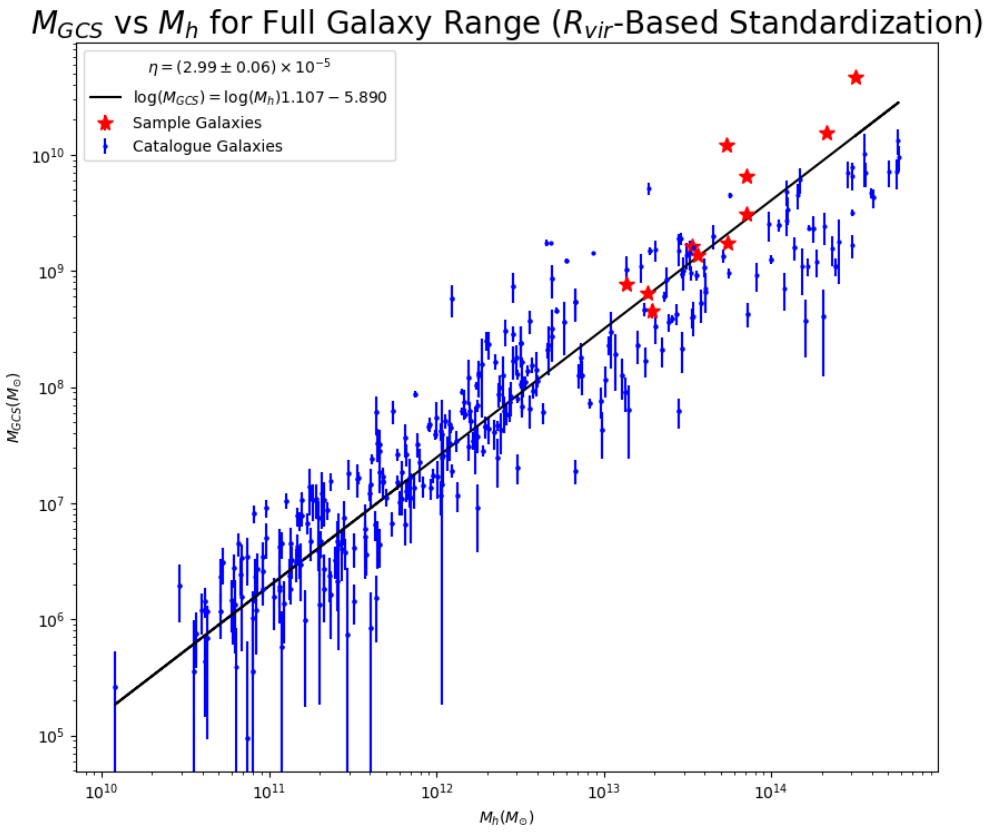

FIGURE 3.4: M_{GCS} determined from R_{vir} standardization plotted against M_h for the galaxies in the sample (red stars) and for the galaxies in literature catalogues (Harris et al. 2013) (blue points) in log-log space.

has lower scatter in the linear fit and follows the fit defined by the lower-mass catalogue better, as seen in figure 3.4. This all translates to a lower uncertainty in the η-value for the R_{vir}-based definition compared to the R_e-based one. In addition, the R_{vir}-based definition is also easier to calculate as it is simply $0.1R_{vir}$ for any galaxy in any sample, while determining the R_e-based definition here was quite dependent on both this specific sample and being able to determine where the breakpoint radii are for each galaxy's GC distribution.

In addition, the R_{vir}-based definition is determined based on values that are

a bit more physically relevant to these GC systems. For instance, R_{vir} is found from M_{vir}, which is essentially the dark matter halo mass that was already calculated and will be compared against the resulting M_{GCS}. The R_e-based definition, however, is determined from the half-light radius, which refers to the radius at which half of the total light of the galaxy is enclosed. For this situation the half-GC-light radius would be more relevant, however that value is not readily available for all galaxies and is more difficult to calculate. As such, it is concluded that the R_{vir}-based definition of GCS size, and the related method of M_{GCS} standardization should be used moving forward. The subsequent discussion and conclusions will be referring to the R_{vir}-based results.

3.1.2 A Note on The Three Most Massive GCSs

The three most numerous and massive GC systems in the high-mass galaxy sample of this research were found to be, in order of ascending masses, 2MASX J13275493-3132187, ESO 383-G076, and ESO 444-G046. This is the case for both GCS size standardization methods, but for the reasons discussed above we will be focusing on the R_{vir}-based values. It should also be noted that the N_{GC} and M_{GCS}-values for ESO 383-G076 and ESO 444-G046 were also found in Harris et al. (2013), and the R_e-based method yields a total GC population number and mass much higher than was found previously, while the R_{vir}-based values are much closer to what was measured previously. This is likely due to the fact that ESO 383-G076, as can be seen in figure 2.8 is much more elliptical than the other galaxies in this research sample, and as such its effective radius is much larger than for the other galaxies examined. ESO 383-G076's virial radius, on the other hand, is dependent on the galaxy's virial mass, rather than the light distribution of the galaxy, and is effected much less by the ellipticity. This is yet another example of why the R_{vir}-based standardization method is preferred.

The most numerous GCS known is that of NGC 6166, which was found to have $N_{GC} = 39000 \pm 2000$ within a radius of the GC system defined as 250kpc. However, it

should also be noted that it is possible that this N_{GC} may be an over estimate due to the large GCS radius that was assumed, thus including a large contribution from the galaxy cluster's intracluster medium. This system should also be re-evaluated using the $0.1R_{vir}$ standardization for further investigation. The most numerous GCS in the high-mass galaxy sample in this research is that of ESO 444-G046 with $N_{GC} = 30566 \pm 644$, which is a slightly smaller number estimate than was found by Harris et al. (2013), but is still in agreement that it is the next most numerous GCS known. This research's GCS number estimates then puts 2MASX J13275493-3132187 and ESO 383-G076 at the fourth and fifth most numerous GC systems known, surpassing the Harris et al. (2013) estimate of A2107 BCG's N_{GC} (found to be 27000 ± 1300). If the large N_{GC} estimate for NGC 6166 is assumed to be an over estimate, or treated as an outlier, combined observational evidence indicates that the GC populations of the most massive known galaxies appear to top out at ~ 30000 GCs.

Chapter 4

Discussion and Conclusions

This chapter will discuss the results laid out in chapter 3 and compare them to the literature work on the $M_{GCS} - M_h$ relation. This chapter will also outline the future work that can be done based on this research, both in terms of new methodology and in terms of what galaxies and in which mass ranges should be investigated next to gain insight into this relation.

4.1 Discussion

As was discussed in chapter 1, section 1.2, the $M_{GCS} - M_h$ ratio has been found observationally to fall within 2.5×10^{-5} and 4.0×10^{-5}. In this research the η-value determined from the sample of high-mass galaxies alone was found to be slightly higher than this range, however the η-value determined from the high-mass sample combined with catalogue galaxies falls well within this established range. The higher than expected η-value for the high-mass sample alone is most likely due simply to the small sample size of only eleven galaxies.

As was discussed in chapter 1, section 1.2.2, there have been some literature predictions in recent years that the $M_{GCS} - M_h$ relation may not be entirely linear for all galaxy masses (El-Badry et al. 2019, Choksi and Gnedin 2019, Bastian et al.

2020). Although these predictions focus heavily on galaxies with dark matter halo masses below $\sim 5 \times 10^{11} M_{\odot}$, as there are very few galaxies in this range that have had their M_h-values determined, it is also possible that this linearity may not completely hold at the extremely high mass end of the relation. The fiducial model created by Choksi and Gnedin (2019), for instance, found that for galaxies with $M_h \gtrsim 10^{13} M_{\odot}$, when the contribution of GCs formed in satellite systems and accreted by the host galaxy is ignored, the M_{GCS}-values of these galaxies can be noticeably lower than expected from linearity, found by Choksi and Gnedin (2019) to be as high as a factor of 0.3 dex.

This research finds, however, that this sample of eleven high-mass galaxies does indeed follow the same linear fit as the lower-mass galaxies taken from the Harris et al. (2013) catalogue. Adding this sample to the catalogue slightly increased the steepness of the linear fit, but also decreased the uncertainty in η, better constraining both the behaviour of the $M_{GCS}-M_h$ relation at high masses, and the relation overall, as intended.

This result is consistent with the predictions from both El-Badry et al. (2019) and Choksi and Gnedin (2019), however El-Badry et al. (2019) argue that finding a constant linear $M_{GCS} - M_h$ relation at halo masses above $10^{11.5} M_{\odot}$ is expected for a wide range of models of GC formation due to the central limit theorem. They argue that observations of a linear $M_{GCS} - M_h$ relation at $z = 0$ for high-mass galaxies, as is the case for this research, should not be considered clear evidence of a linear relations at formation.

On the other hand, while Choksi and Gnedin (2019) accept that observing a linear $M_{GCS} - M_h$ relation at $z = 0$ cannot explicitly prove the existence of this relation at high redshifts, they argue that it also does not preclude it. Choksi and Gnedin (2019) go on to state that a linear relation is still seen at high redshifts in their model since they defined thair cluster formation rate as $M_{tot} \propto M_g$, as motivated by the results of early cosmological simulations by Kravtsov and Gnedin (2005), where M_g is the galaxy's

cold gas mass. This would imply that these massive galaxies in our sample have a large proportion of their GCSs made of accreted GCs from satellite galaxies, and that at lower redshifts major mergers play a more significant role in triggering GC formation than for lower-mass galaxies. This is shown by figure 4.1 from Choksi and Gnedin (2019), which compares their fiducial model which accounts for all GCs in the systems to the same model with accreted GCs removed, where a more significant difference can be seen at high masses.

4.2 Future Work

One of the uncertainties in this work that could not be fully corrected for was the influence of the GC population of large satellite galaxies on the GC population of the target galaxy. All galaxies in the sample had a number of small satellite galaxies in the target image being analyzed, however 2MASX J13275493-3132187 and ESO 509-G020 each had a significant satellite galaxy in their image, as can be seen in figure 2.8. In order to remove these significant satellite galaxies, the same method was applied to them as was applied to the smaller satellites, by just removing all objects within a certain radius of the satellite galaxy. Although this method works well for the smaller satellites, for the larger ones the distributions of both their and the target galaxy's GCs can be related in a more complex way. So although this method works well enough for this research, it can both remove GCs that may be associated with the target galaxy or leave behind GCs associated with the major satellite galaxy, which is not ideal.

A more sophisticated method of removing these significant satellite galaxies would allow the distributions of both the central and satellite galaxies to be deduced simultaneously so the GCs associated with the satellite can be removed more accurately, down to small areas and individual objects. This would redefine the expression for the total GC density of the combined systems at any given point as equation 4.1. Here $\sigma_1(r_1)$ is the density associated with the target galaxy at a radius from the target galaxy,

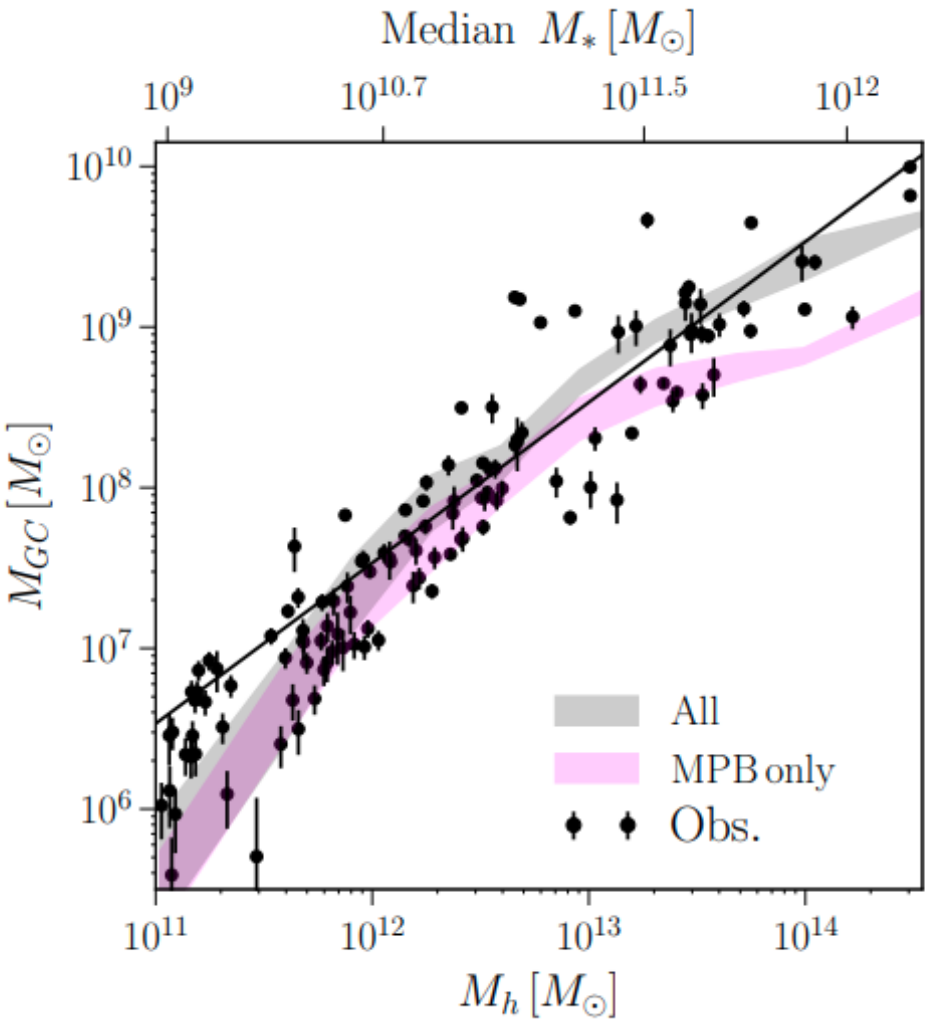

FIGURE 4.1: M_{GCS} vs M_h for observed values represented by the black points, and for the fiducial model done by Choksi and Gnedin (2019), where gray is for the complete model, and magenta is for the model excluding any contribution from accreted GCs. Reprinted from N. Choksi and O. Y. Gnedin (Oct. 2019). Origins of scaling relations of globular cluster systems. *Monthly Notices of the Royal Astronomical Society* 488(4), 5409–5419.

$\sigma_2(r_2)$ is the density associated with the satellite galaxy at a radius from the satellite galaxy, and r is an arbitrary point simultaneously r_1 away from the target galaxy and r_2 away from the satellite galaxy. Once this can be defined, we would aim to isolate and

determine $\sigma(r_1)$.

$$\sigma_{tot}(r) = \sigma_1(r_1) + \sigma_2(r_2) + \sigma_{background} \tag{4.1}$$

One method that could achieve this would be to use Voronoi cells in a similar way as was done in Lahén et al. (2020). Voronoi cells create regions within an image where a value (number of GCs here) is constant with varying area, as opposed to a grid, which has cells of constant area and varying values associated with them (Okabe et al. 1992). This would allow a more precise removal of contaminating GCs around satellite galaxies since at extremely high densities, such as those found around satellite galaxies, Voronoi cells can become small enough to enclose single objects. This, in turn, would ensure that such large portions of the target images do not need to be completely removed, giving a more complete distribution of the target galaxy's GC population. Achieving this will be useful not only in work related to this research, but also in any research that needs to determine local number density down to the level of single objects, reducing the need to average over large areas.

Another future application of this research would be to apply the R_{vir}-based GCS size standardization to more massive galaxies, including those in the Harris et al. (2013) catalogue. As can be seen in figures 3.3 and 3.4, the ten most massive galaxies in the catalogue have GCS masses lower than expected based on the linear fit. This could be due to the fact that the radii of their GC systems was underestimated and left out accreted GCs on the outskirts of the galaxies. Re-calculating these galaxies' GCS masses can determine whether or not this is the case, and if these galaxies' masses are consistent with those in this research's sample. Using this method of standardization will also be useful going forward as more BCGs are added to our understanding of the $M_{GCS} - M_h$ relation.

The next steps in better constraining the $M_{GCS} - M_h$ relation in general would

be to better understand the behaviour at the opposite extreme mass end, and investigate dwarf galaxies. El-Badry et al. (2019) predicts that galaxies with halo masses less than $10^{11} M_{\odot}$ would have a steeper slope of the $M_{GCS} - M_h$ relation than for galaxies with higher masses. However, observaionally Forbes et al. (2018) found that the linear shape of the $M_{GCS} - M_h$ relation holds down to at least $10^9 M_{\odot}$, although at these lowest masses the scatter increases significantly.

This increase in scatter is due to the fact that the low-mass end of this relation presents a specific challenge, as it is quite difficult to estimate halo masses of dwarf galaxies. One of the reasons why this is the case is because the $M_{\star} - M_h$ relation normally used to estimate the halo mass becomes much less well-known at extremely low masses, so most of the previous research into the low-mass end is done with simulated galaxies, rather than observational data. In order to properly constrain the low-mass end of the $M_{GCS} - M_h$ relation, alternative methods to determine halo mass will need to be implemented. Because there exists no relation that can be applied across all dwarf galaxies to determine halo mass, as there was for the high mass galaxies, appropriate methods need to be used for different galaxies, as is allowed by the circumstances.

Forbes et al. (2018) utilized the stellar and HI gas kinematics, along with a model-based extrapolation out to very large radii of various dwarf galaxies to determine their halo masses. This proves to be a promising method to be extended to more dwarf galaxies in this research. Being able to determine if the $M_{GCS} - M_h$ relation remains constant at these low masses can help us gain important insight into the GC formation mechanisms of dwarf galaxies, in addition to the role dark matter may play. As we begin to identify more dwarf galaxies with very little dark matter, or seemingly lack dark matter entirely, such as NGC1052–DF2 (van Dokkum et al. 2018), this raises more questions about what the link between GCs and dark matter can be. A larger and more standardized analysis of these extremely low-mass galaxies can also hopefully lower the uncertainty in these mass estimates.

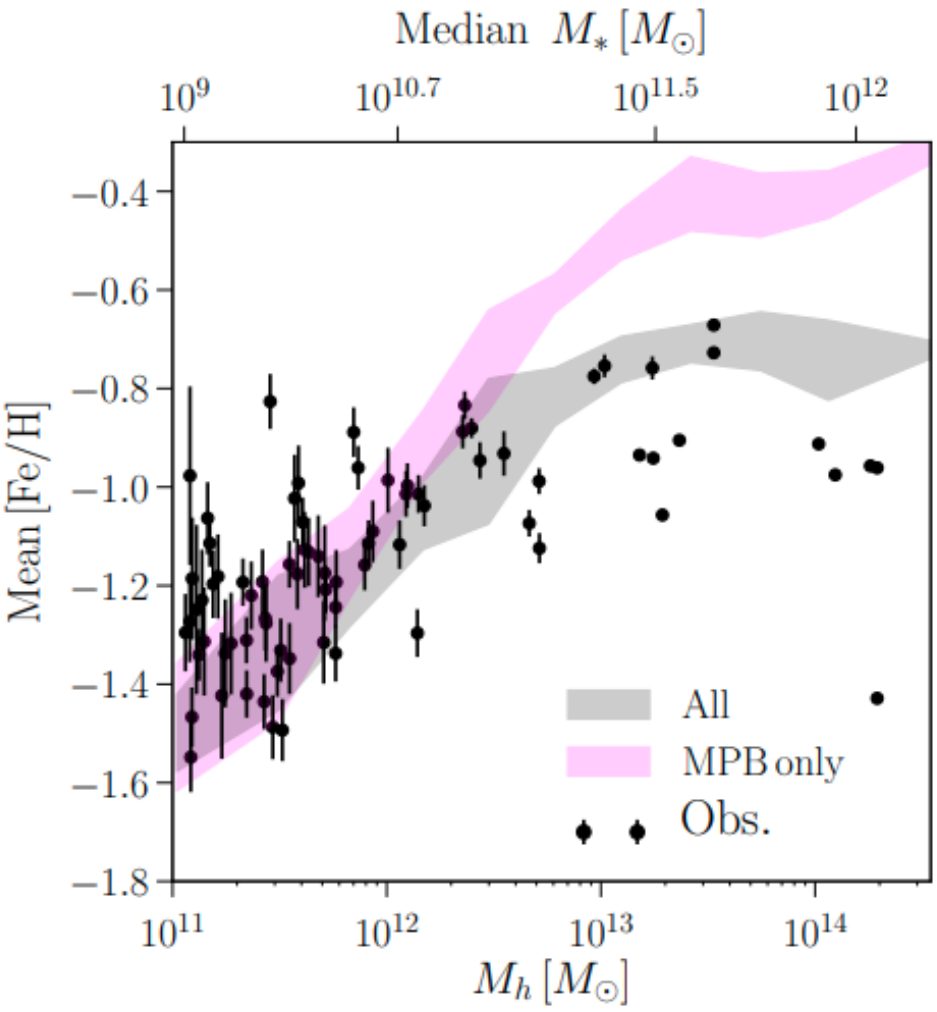

FIGURE 4.2: Mean GCS [Fe/H] vs M_h for observed values represented by the black points, and for the fiducial model done by Choksi and Gnedin (2019), where gray is for the complete model, and magenta is for the model excluding any contribution from accreted GCs. Reprinted from N. Choksi and O. Y. Gnedin (Oct. 2019). Origins of scaling relations of globular cluster systems. *Monthly Notices of the Royal Astronomical Society* 488(4), 5409–5419.

Another limitation of this research is that the images that were analyzed were taken in only one filter, F814W, which means the colour, and by extension metallicity, of the GCs could not be determined. GC metallicity can act as a proxy for determining if a GC was formed in-situ or ex-situ of its current host galaxy, as was shown in Choksi

and Gnedin (2019), where accreted GCs tend to have lower [Fe/H] values and vice versa for massive galaxies. This difference in mean GCS metallicity when considering and ignoring accreted GCs is shown in figure 4.2. In future work, it would be useful to analyze galaxies with an additional blue filter in order to be able to determine how many of their GCs were most likely accreted based on their metallicities, and if there is any clear metallicity distribution pattern. This will allow the results to be more thoroughly compared to literature predictions.

4.3 Conclusions

To summarize, this work expands upon our understanding of the $M_{GCS} - M_h$ relation, specifically better constraining our understanding of the relation's behaviour at the high mass end, which has been lacking in data compared to the lower mass range. A sample of eleven massive BCGs were selected to be analyzed and have their GCS and dark matter halo masses determined. The numbers of GCs in these galaxies were determined by finding the GC radial distribution through photometry and then integrating out to $0.1R_{vir}$, as a standard. This was then converted to the total mass of the GCS by multiplying this number by the average mass of a single GC in the galaxy, determined based on the galaxy's total luminosity, shown in equation 2.3. The halo masses of the sample were determined using a relationship between total stellar mass and halo mass, equation 2.12, that holds strongly for galaxies with high masses such as the ones in this sample.

The shape and steepness of the relationship between these masses were then determined by plotting the masses against each other for the galaxies in the sample, both for the sample by itself and when added to a catalogue of 303 galaxies over a much wider range of masses. It was found that the η-values calculated from the GCS masses determined using R_{vir}-based standardization had less scatter than those determined using R_e-based standardization, and so these R_{vir}-based results are the ones that are

focused on. The η-value from the sample of high-mass galaxies alone was found to be $\eta = (6.84 \pm 0.10_{internal} \pm 1.37_{external}) \times 10^{-5}$, which although is higher than the previously found literature range, this discrepancy is likely due to the small sample size. The η-value found from the sample combined with the catalogue galaxies was found to be much more in-line with literature predictions, at $\eta = (2.99 \pm 0.06) \times 10^{-5}$.

This new η-value is slightly higher than the value from the catalogue galaxies alone, $\eta = (2.87 \pm 0.11) \times 10^{-5}$, but also has a reduced uncertainty. It was found that the high mass sample galaxies did not deviate from the linear shape of the relation that the lower mass galaxies followed. This suggests that these high mass galaxies have a large number of accreted GCs in their GC systems, and that galaxy mergers at late redshift play a larger role in their GC formation mechanisms than for lower mass galaxies, as was predicted by El-Badry et al. (2019) and Choksi and Gnedin (2019).

Appendix A

Dolphot Parameter File Example

```
Nimg = 22
img0_file = f814w_combined_drc.chip1
img1_file = j95t07waq_flc.chip1
img2_file = j95t07wbq_flc.chip1
img3_file = j95t07wdq_flc.chip1
img4_file = j95t07wfq_flc.chip1
img5_file = j95t07whq_flc.chip1
img6_file = j95t07wjq_flc.chip1
img7_file = j95t07wlq_flc.chip1
img8_file = j95t07wnq_flc.chip1
img9_file = j95t07wpq_flc.chip1
img10_file = j95t07wrq_flc.chip1
img11_file = j95t07wtq_flc.chip1
img12_file = j95t07wvq_flc.chip1
img13_file = j95t07wxq_flc.chip1
img14_file = j95t07wzq_flc.chip1
img15_file = j95t07x1q_flc.chip1
img16_file = j95t08azq_flc.chip1
img17_file = j95t08b0q_flc.chip1
img18_file = j95t08b2q_flc.chip1
img19_file = j95t08b4q_flc.chip1
img20_file = j95t08b6q_flc.chip1
img21_file = j95t08b8q_flc.chip1
img22_file = j95t08baq_flc.chip1
#
img_shift = 0 0          #shift relative to reference
img_xform = 1 0 0        #scale, distortion, and rotation
img_PSFa = 3 0 0 0 0 0 0  #PSF XX term (flt)
img_PSFb = 3 0 0 0 0 0 0  #PSF YY term (flt)
img_PSFc = 0 0 0 0 0 0 0  #PSF XY term (flt)
img_RAper = 6.0          #photometry apeture size (flt)
img_RChi = -1            #Aperture for determining centroiding (flt); if <=0 use RAper
img_RSky = 15 25         #radii defining sky annulus (flt>=RAper+0.5)
img_RPSF = 15            #PSF size (int>0)
img_aprad = 15           #radius for aperture correction
```

```
img_apsky = 25 30       #sky annulus for aperture correction
#
# The following photometers affect the finding and measurement of stars
photsec =               #section: group, chip, (X,Y)0, (X,Y)1
RCentroid = 2           #centroid box size (int>0)
SigFind = 3.0           #sigma detection threshold (flt)
SigFindMult = 0.85      #Multiple for quick-and-dirty photometry (flt>0)
SigFinal = 3.5          #sigma output threshold (flt)
MaxIT = 10              #maximum iterations (int>0)
FPSF = Lorentz          #PSF function (str/Gauss,Lorentz,Lorentz^2,G+L)
PSFPhot = 1             #photometry type (int/0=aper,1=psf,2=wtd-psf)
PSFPhotIt = 1           #number of iterations in PSF-fitting photometry (int>=0)
FitSky = 2              #fit sky? (int/0=no,1=yes,2=small,3=with-phot)
SkipSky = 1             #spacing for sky measurement (int>0)
SkySig = 2.25           #sigma clipping for sky (flt>=1)
NegSky = 1              #allow negative sky values? (0=no,1=yes)
NoiseMult = 0.10        #noise multiple in imgadd (flt)
FSat = 0.999            #fraction of saturate limit (flt)
Zero = 25.0             #zeropoint for 1 DN/s (flt)
PosStep = 0.25          #search step for position iterations (flt)
dPosMax = 3.0           #maximum single-step in position iterations (flt)
RCombine = 1.5          #minimum separation for two stars for cleaning (flt)
SigPSF = 5.0            #min S/N for psf parameter fits (flt)
PSFStep = 0.25          #stepsize for PSF
MinS = 1.0              #minimum FWHM for good star (flt)
MaxS = 5.0              #maximum FWHM for good star (flt)
MaxE = 0.5              #maximum ellipticity for good star (flt)
#
# Settings to enable/disable features
UseWCS = 1              #use WCS info in alignment (int 0=no, 1=shift/rotate/scale, 2=full)
Align = 3               #align images? (int 0=no,1=const,2=lin,3=cube)
AlignIter = 2           #number of iterations on alignment? (int>0)
AlignTol = 0            #number of pixels to search in preliminary alignment (flt>=0)
AlignStep = 1           #stepsize for preliminary alignment search (flt>0)
AlignOnly = 0           #exit after alignment
Rotate = 1              #allow cross terms in alignment? (int 0=no, 1=yes)
SubResRef = 1           #subpixel resolution for reference image (int>0)
SecondPass = 1          #second pass finding stars (int 0=no,1=yes)
SearchMode = 1          #algorithm for astrometry (0=max SNR/chi, 1=max SNR)
Force1 = 0              #force type 1/2 (stars)? (int 0=no,1=yes)
EPSF = 1                #allow elliptical PSFs in parameter fits (int 0=no,1=yes)
PSFsol = 1              #Analytic PSF solution (int -1=none, 0=con, 1=lin, 2=quad)
PSFres = 1              #make PSF residual image? (int 0=no,1=yes)
psfstars =              #Coordinates of PSF stars
psfoff = 0.0            #coordinate offset (PSF system - dolphot system)
ApCor = 1               #find/make aperture corrections? (int 0=no,1=yes)
SubPixel = 1            #subpixel PSF calculation (int>0)
FakeStars =             #file with fake star input data
FakeOut =               #file with fake star output data (default=phot.fake)
FakeMatch = 3.0         #maximum separation between input and recovered star (flt>0)
FakePSF = 2.0           #assumed PSF FWHM for fake star matching
FakeStarPSF = 1         #use PSF residuals in fake star tests? (int 0=no,1=yes)
RandomFake = 1          #apply Poisson noise to fake stars? (int 0=no,1=yes)
```

```
FakePad = 0              #minimum distance of fake star from any chip edge to be used
UsePhot =                #if defined, use alignment, PSF, and aperture corr from photometry
DiagPlotType =           #format to generate diagnostic plots (PNG, GIF, PS)
xytfile =                #position file for warmstart (str)
xytpsf =                 #reference PSF for image subtraction
VerboseData = 0          #to write all displayed numbers to a .data file
#
# Flags for HST modes
ForceSameMag = 0         #force same count rate in images with same filter? (int 0=no, 1=yes)
FlagMask = 4             #photometry quality flags to reject when combining magnitudes
CombineChi = 0           #combined magnitude weights uses chi? (int 0=no, 1=yes)
WFPC2useCTE = 1          #apply CTE corrections on WFPC2 data? (int 0=no, 1=yes)
ACSuseCTE = 0            #apply CTE corrections on ACS data? (int 0=no, 1=yes)
WFC3useCTE = 0           #apply CTE corrections on WFC3 data? (int 0=no, 1=yes)
ACSpsfType = 0           #use Anderson PSF cores? (int 0=no, 1=yes)
WFC3UVISpsfType = 0      #use Anderson PSF cores? (int 0=no, 1=yes)
WFC3IRpsfType = 0        #use Anderson PSF cores? (int 0=no, 1=yes)
InterpPSFlib = 1         #interpolate PSF library spatially
#
# Other flags not recommended for most users
#img_ref2img =           #high order terms for conversion between image (distortion-corrected
                         #if HST) and reference
```

Bibliography

El-Badry, K., Quataert, E., Weisz, D. R., Choksi, N., and Boylan-Kolchin, M. (Feb. 2019). The formation and hierarchical assembly of globular cluster populations. *Monthly Notices of the Royal Astronomical Society* 482(4), 4528–4552.

Bastian, N., Pfeffer, J., Kruijssen, J. M. D., Crain, R. A., Trujillo-Gomez, S., and Reina-Campos, M. (Oct. 2020). The globular cluster system mass-halo mass relation in the E-MOSAICS simulations. *Monthly Notices of the Royal Astronomical Society* 498(1), 1050–1061.

Beasley, M. A. (2020). Globular Cluster Systems and Galaxy Formation. In: *Reviews in Frontiers of Modern Astrophysics; From Space Debris to Cosmology*, 245–277.

Bekki, K., Yahagi, H., Nagashima, M., and Forbes, D. A. (July 2008). The origin of globular cluster systems from cosmological simulations. *Monthly Notices of the Royal Astronomical Society* 387(3), 1131–1148.

Bell, E. F., McIntosh, D. H., Katz, N., and Weinberg, M. D. (Dec. 2003). The Optical and Near-Infrared Properties of Galaxies. I. Luminosity and Stellar Mass Functions. *Astrophysical Journal Supplement Series* 149(2), 289–312.

Blakeslee, J. (July 2004). *Streaming Towards Shapley: The Mass of the Richest Galaxy Concentration in the Local Universe*. HST Proposal.

Blakeslee, J. P. (Oct. 1999). Globular Clusters in Dense Clusters of Galaxies. *Astrophysical Journal* 118(4), 1506–1525.

Blakeslee, J. P., Tonry, J. L., and Metzger, M. R. (Aug. 1997). Globular Clusters in 19 Northern Abell Clusters. *Astrophysical Journal* 114, 482–506.

Boylan-Kolchin, M. (Dec. 2017). The globular cluster-dark matter halo connection. *Monthly Notices of the Royal Astronomical Society* 472(3), 3120–3130.

Choksi, N. and Gnedin, O. Y. (Oct. 2019). Origins of scaling relations of globular cluster systems. *Monthly Notices of the Royal Astronomical Society* 488(4), 5409–5419.

Coupon, J., Arnouts, S., van Waerbeke, L., Moutard, T., Ilbert, O., van Uitert, E., Erben, T., Garilli, B., Guzzo, L., Heymans, C., Hildebrandt, H., Hoekstra, H., Kilbinger, M., Kitching, T., Mellier, Y., Miller, L., Scodeggio, M., Bonnett, C., Branchini, E., Davidzon, I., De Lucia, G., Fritz, A., Fu, L., Hudelot, P., Hudson, M. J., Kuijken, K., Leauthaud, A., Le Fèvre, O., McCracken, H. J., Moscardini, L., Rowe, B. T. P., Schrabback, T., Semboloni, E., and Velander, M. (May 2015). The galaxy-halo connection from a joint lensing, clustering and abundance analysis in the CFHTLenS/VIPERS field. *Monthly Notices of the Royal Astronomical Society* 449(2), 1352–1379.

Diemand, J., Madau, P., and Moore, B. (Dec. 2005). The distribution and kinematics of early high-σ peaks in present-day haloes: implications for rare objects and old stellar populations. *Monthly Notices of the Royal Astronomical Society* 364(2), 367–383.

Dolphin, A. (Jan. 2013). *DOLPHOT User's Guide*. English. Version 2.0.

Dolphin, A. E. (Oct. 2000). WFPC2 Stellar Photometry with HSTPHOT. *Publications of the Astronomical Society of the Pacific* 112(776), 1383–1396.

Doppel, J. E., Sales, L. V., Navarro, J. F., Abadi, M. G., Peng, E. W., Toloba, E., and Ramos-Almendares, F. (Apr. 2021). Globular clusters as tracers of the dark matter content of dwarfs in galaxy clusters. *Monthly Notices of the Royal Astronomical Society* 502(2), 1661–1677.

Forbes, D. A., Read, J. I., Gieles, M., and Collins, M. L. M. (Dec. 2018). Extending the globular cluster system-halo mass relation to the lowest galaxy masses. *Monthly Notices of the Royal Astronomical Society* 481(4), 5592–5605.

Gallagher, J. S., Faber, S. M., and Burstein, D. (Feb. 1980). B-V color profiles of the luminous elliptical galaxies NGC 4472 and NGC 5846 and the cD galaxy NGC 6166. *Astrophysical Journal* 235, 743–748.

Georgiev, I. Y., Puzia, T. H., Goudfrooij, P., and Hilker, M. (Aug. 2010). Globular cluster systems in nearby dwarf galaxies - III. Formation efficiencies of old globular clusters. *Monthly Notices of the Royal Astronomical Society* 406(3), 1967–1984.

Harris, W. E. and Racine, R. (Jan. 1979). Globular clusters in galaxies. 17, 241–274.

Harris, W. E., Blakeslee, J. P., and Harris, G. L. H. (Feb. 2017). Galactic Dark Matter Halos and Globular Cluster Populations. III. Extension to Extreme Environments. *Astrophysical Journal* 836(1) 67, 67.

Harris, W. E., Blakeslee, J. P., Whitmore, B. C., Gnedin, O. Y., Geisler, D., and Rothberg, B. (Jan. 2016). Globular Cluster Systems in Brightest Cluster Galaxies. II. NGC 6166. *Astrophysical Journal* 817(1) 58, 58.

Harris, W. E., Harris, G. L., and Hudson, M. J. (June 2015). Dark Matter Halos in Galaxies and Globular Cluster Populations. II. Metallicity and Morphology. *Astrophysical Journal* 806(1) 36, 36.

Harris, W. E., Harris, G. L., and Alessi, M. (Aug. 2013). A Catalog of Globular Cluster Systems: What Determines the Size of a Galaxy's Globular Cluster Population? *Astrophysical Journal* 772(2) 82, 82.

Harris, W. E., Morningstar, W., Gnedin, O. Y., O'Halloran, H., Blakeslee, J. P., Whitmore, B. C., Côté, P., Geisler, D., Peng, E. W., Bailin, J., Rothberg, B., Cockcroft, R., and Barber DeGraaff, R. (Dec. 2014). Globular Cluster Systems in Brightest Cluster Galaxies: A Near-universal Luminosity Function? *Astrophysical Journal* 797(2) 128, 128.

Harris, W. E., Remus, R.-S., Harris, G. L. H., and Babyk, I. V. (Dec. 2020). Measuring Dark Matter in Galaxies: The Mass Fraction within Five Effective Radii. *Astrophysical Journal* 905(1) 28, 28.

Howard, C. S., Pudritz, R. E., and Harris, W. E. (June 2018). A universal route for the formation of massive star clusters in giant molecular clouds. *Nature Astronomy* 2, 725–730.

Hudson, M. J., Gillis, B. R., Coupon, J., Hildebrandt, H., Erben, T., Heymans, C., Hoekstra, H., Kitching, T. D., Mellier, Y., Miller, L., Van Waerbeke, L., Bonnett, C., Fu, L., Kuijken, K., Rowe, B., Schrabback, T., Semboloni, E., van Uitert, E., and Velander, M. (Feb. 2015). CFHTLenS: co-evolution of galaxies and their dark matter haloes. *Monthly Notices of the Royal Astronomical Society* 447(1), 298–314.

Hudson, M. J., Harris, G. L., and Harris, W. E. (May 2014). Dark Matter Halos in Galaxies and Globular Cluster Populations. *Astrophysical Journal Letters* 787(1) L5, L5.

Hudson, M. J. and Robison, B. (July 2018). The correlation between the sizes of globular cluster systems and their host dark matter haloes. *Monthly Notices of the Royal Astronomical Society* 477(3), 3869–3885.

Huxor, A. P., Ferguson, A. M. N., Tanvir, N. R., Irwin, M. J., Mackey, A. D., Ibata, R. A., Bridges, T., Chapman, S. C., and Lewis, G. F. (June 2011). Exploring the properties of the M31 halo globular cluster system. 414(1), 770–780.

Jordán, A., McLaughlin, D. E., Côté, P., Ferrarese, L., Peng, E. W., Mei, S., Villegas, D., Merritt, D., Tonry, J. L., and West, M. J. (July 2007). The ACS Virgo Cluster Survey. XII. The Luminosity Function of Globular Clusters in Early-Type Galaxies. *Astrophysical Journal Supplement Series* 171(1), 101–145.

Kravtsov, A. V. and Gnedin, O. Y. (Apr. 2005). Formation of Globular Clusters in Hierarchical Cosmology. *Astrophysical Journal* 623(2), 650–665.

Lahén, N., Naab, T., Johansson, P. H., Elmegreen, B., Hu, C.-Y., and Walch, S. (Nov. 2020). Structure and Rotation of Young Massive Star Clusters in a Simulated Dwarf Starburst. *Astrophysical Journal* 904(1) 71, 71.

Li, H. and Gnedin, O. Y. (Nov. 2014). Modeling the Formation of Globular Cluster Systems in the Virgo Cluster. *Astrophysical Journal* 796(1) 10, 10.

Lim, J., Wong, E., Ohyama, Y., Broadhurst, T., and Medezinski, E. (Feb. 2020). Sustained formation of progenitor globular clusters in a giant elliptical galaxy. *Nature Astronomy* 4, 153–158.

Madau, P., Lupi, A., Diemand, J., Burkert, A., and Lin, D. N. C. (Feb. 2020). Globular Cluster Formation from Colliding Substructure. *Astrophysical Journal* 890(1) 18, 18.

Moore, B., Diemand, J., Madau, P., Zemp, M., and Stadel, J. (May 2006). Globular clusters, satellite galaxies and stellar haloes from early dark matter peaks. *Monthly Notices of the Royal Astronomical Society* 368(2), 563–570.

Okabe, A., Boots, B., and Sugihara, K. (1992). *Spatial tessellations. Concepts and Applications of Voronoi diagrams.*

Peebles, P. J. E. and Dicke, R. H. (Dec. 1968). Origin of the Globular Star Clusters. *Astrophysical Journal* 154, 891.

Pfeffer, J., Kruijssen, J. M. D., Crain, R. A., and Bastian, N. (Apr. 2018). The E-MOSAICS project: simulating the formation and co-evolution of galaxies and their star cluster populations. 475(4), 4309–4346.

Prole, D. J., Hilker, M., van der Burg, R. F. J., Cantiello, M., Venhola, A., Iodice, E., van de Ven, G., Wittmann, C., Peletier, R. F., Mieske, S., Capaccioli, M., Napolitano, N. R., Paolillo, M., Spavone, M., and Valentijn, E. (Apr. 2019). Halo mass estimates from the globular cluster populations of 175 low surface brightness galaxies in the Fornax cluster. *Monthly Notices of the Royal Astronomical Society* 484(4), 4865–4880.

Reina-Campos, M. and Kruijssen, J. M. D. (Aug. 2017). A unified model for the maximum mass scales of molecular clouds, stellar clusters and high-redshift clumps. *Monthly Notices of the Royal Astronomical Society* 469(2), 1282–1298.

Ryon, J. E. (2019). *Advanced Camera for Surveys Instrument Handbook for Cycle 27 v. 18.0.*

Spitler, L. R. and Forbes, D. A. (Jan. 2009). A new method for estimating dark matter halo masses using globular cluster systems. *Monthly Notices of the Royal Astronomical Society* 392(1), L1–L5.

Spitler, L. R., Forbes, D. A., Strader, J., Brodie, J. P., and Gallagher, J. S. (Mar. 2008). The connection between globular cluster systems and their host galaxy and environment: a case study of the isolated elliptical NGC 821. *Monthly Notices of the Royal Astronomical Society* 385(1), 361–380.

Stetson, P. B. (Mar. 1987). DAOPHOT: A Computer Program for Crowded-Field Stellar Photometry. *Publications of the Astronomical Society of the Pacific* 99, 191.

Trenti, M., Padoan, P., and Jimenez, R. (Aug. 2015). The Relative and Absolute Ages of Old Globular Clusters in the LCDM Framework. *Astrophysical Journal Letters* 808(2) L35, L35.

van Dokkum, P., Danieli, S., Cohen, Y., Merritt, A., Romanowsky, A. J., Abraham, R., Brodie, J., Conroy, C., Lokhorst, D., Mowla, L., O'Sullivan, E., and Zhang, J. (Mar. 2018). A galaxy lacking dark matter. *Nature* 555(7698), 629–632.

VandenBerg, D. A., Brogaard, K., Leaman, R., and Casagrande, L. (Oct. 2013). The Ages of 55 Globular Clusters as Determined Using an Improved ΔV_{TO}^{HB} Method along with Color-Magnitude Diagram Constraints, and Their Implications for Broader Issues. *Astrophysical Journal* 775(2) 134, 134.

Villegas, D., Jordán, A., Peng, E. W., Blakeslee, J. P., Côté, P., Ferrarese, L., Kissler-Patig, M., Mei, S., Infante, L., Tonry, J. L., and West, M. J. (July 2010). The ACS Fornax Cluster Survey. VIII. The Luminosity Function of Globular Clusters in Virgo and Fornax Early-type Galaxies and Its Use as a Distance Indicator. *Astrophysical Journal* 717(2), 603–616.